NASA Contractor Report CR-175112

NASA-CR-175112
19860017811

STRUCTURAL TAILORING OF ENGINE BLADES (STAEBL)

Theoretical Manual

K. Brown

Prepared for
NASA-Lewis Research Center
Under Contract NAS3-23697
June 1986

National Aeronautics and
Space Administration

Lewis Research Center
Cleveland, Ohio 44135
AC 216 433-4000

UNITED TECHNOLOGIES
PRATT&WHITNEY

400 Main Street
East Hartford, Connecticut 06108

In reply please refer to:
KWB:dla:(0163k); MS 163-10
Ref. No. PWA-5774-40, NASA CR-175112

June 23, 1986

To: National Aeronautics and Space Administration
Lewis Research Center
21000 Brookpark Road
Cleveland, Ohio 44135

Attention: Mr. Chris Chamis, Program Manager
Bldg. 49 Room 211
Mail Stop 49-6

Subject: Theoretical Manual for the Structural Tailoring of Engine Blades (STAEBL) Program

Reference: Contract NAS3-22525

Mr. Chamis:

We are pleased to submit six copies of the Theoretical Manual in fulfillment of the terms of the referenced contract.

Sincerely yours,

UNITED TECHNOLOGIES CORPORATION
Pratt & Whitney Group
Engineering Division

Kenneth W. Brown
Program Manager

cc: Administrative Contracting Officer
Air Force Plant Representative Office
UTC/Pratt & Whitney
East Hartford, Connecticut 06108

1. Report No.	2. Government Accession No.	3. Recipient's Catalog No.
NASA CR- 175112		

4. Title and Subtitle	5. Report Date
Structural Tailoring of Engine Blades (STAEBL) Theoretical Manual	March 1985
	6. Performing Organization Code
7. Author(s)	8. Performing Organization Report No.
K. W. Brown	PWA-5774-40
	10. Work Unit No.
9. Performing Organization Name and Address United Technologies Corporation Pratt & Whitney Aircraft Group Commercial Products Division East Hartford, CT 06108	11. Contract or Grant No. NAS3-22525
	13. Type of Report and Period Covered Theoretical Manual
12. Sponsoring Agency Name and Address National Aeronautics & Space Administration Washington, DC 20546	14. Sponsoring Agency Code

15. Supplementary Notes Project Managers, C. C. Chamis and M. S. Hirschbein
NASA Lewis Research Center
21000 Brookpark Road, MS 49-8
Cleveland, OH 44135

16. Abstract

This Theoretical Manual includes the theories included in the Structural Tailoring of Engine Blades (STAEBL) computer program which was developed to perform engine fan and compressor blade numerical optimizations. These blade optimizations seek a minimum weight or cost design that satisfies practical blade design constraints, by controlling one to twenty design variables. The STAEBL constraint analyses include blade stresses, vibratory response, flutter, and foreign object damage. Blade design varaibles include airfoil thickness at several locations, blade chord, and construction variables: hole size for hollow blades, and composite material layup for composite blades.

17. Key Words (Suggested by Author(s))	18. Distribution Statement
Special Finite element; Mathematical Optimization; Objective Function; Constraints; Flutter; Forced Vibrations, Impact.	Unclassified, Unlimited

19. Security Classif. (of this report)	20. Security Classif. (of this page)	21. No. of pages	22. Price*
Unclassified	Unclassified		

*For sale by the National Technical Information Service, Springfield, Virginia 22161

STRUCTURAL TAILORING OF ENGINE BLADES (STAEBL)
THEORETICAL MANUAL

Table of Contents

Table of Contents (continued)

List of Illustrations

List of Tables

SECTION 1.0

STAEBL PROGRAM DESCRIPTION

The Structural Tailoring of Engine Blades (STAEBL) computer program was developed to perform engine fan and compressor blade numerical optimizations. These blade optimizations seek a minimum weight or cost design that satisfies realistic blade design constraints, by tuning one to twenty design variables.

The STAEBL constraint analyses include blade stresses, vibratory response, flutter, and foreign object damage. Blade design variables include airfoil thickness at several locations, blade chord, and construction variables: hole size for hollow blades, and composite material layup for composite blades.

A flowchart of the STAEBL procedure is shown in Figure 1. To perform a blade optimization, three component analysis categories are required: an optimization algorithm; approximate analysis procedures for objective function and constraint evaluation; and refined analysis procedures for optimum design validation. The STAEBL computer program contains an executive control module, an optimizer, and all approximate analyses. The optimization algorithm of STAEBL is the COPES/CONMIN (Control Program for Engineering Synthesis/Constrained Minimization) optimization package, which is a proven tool for optimizations with a small to medium (1-20) number of design variables.

The approximate analyses of STAEBL utilize an efficient, coarse mesh, plate finite element blade vibration analysis procedure. The finite element analysis provides blade natural frequencies and mode shapes, stress under centrifugal loads, and blade weight. Additional constraint evaluations, including flutter and foreign object damage calculations, utilize output from the finite element analysis.

Once a candidate optimal design has been found the design should be verified by applying refined analyses to assure that all constraints are satisfied. This level of analysis is not automatically performed by STAEBL, but is left to the user's existing design/analysis system. STAEBL experience has shown that a first optimal candidate design satisfies most constraints, and does not severely violate the remaining constraints. If a constraint is found to be violated, the allowable constraint value must be modified, to reflect the differences between approximate and refined analysis. For each of the cases studied during the STAEBL development effort a fully satisfactory design was found on the second optimal blade design.

To use the blade optimization system, a coordinate description of the initial blade design is required. From that point, STAEBL will change the blade design according to the available blade design variables. Typically, blade geometry variables have consisted of maximum section thickness at five spanwise locations, and blade chord. For the composite blades optimized by STAEBL, additional construction variables are also available. These variables include composite material thickness and orientation, and/or hollow size and location.

The STAEBL system has been applied to several stages of the Energy Efficient Engine, which was designed under NASA Contract NAS3-20646. Fan blades of superhybrid and inlaid hollow construction have been tailored, showing significant potential for design improvements through the application of numerical optimization and these composite constructions. A solid, all titanium compressor blade was also tailored using STAEBL, demonstrating significant blade weight reduction even for a relatively "simple" blade design application.

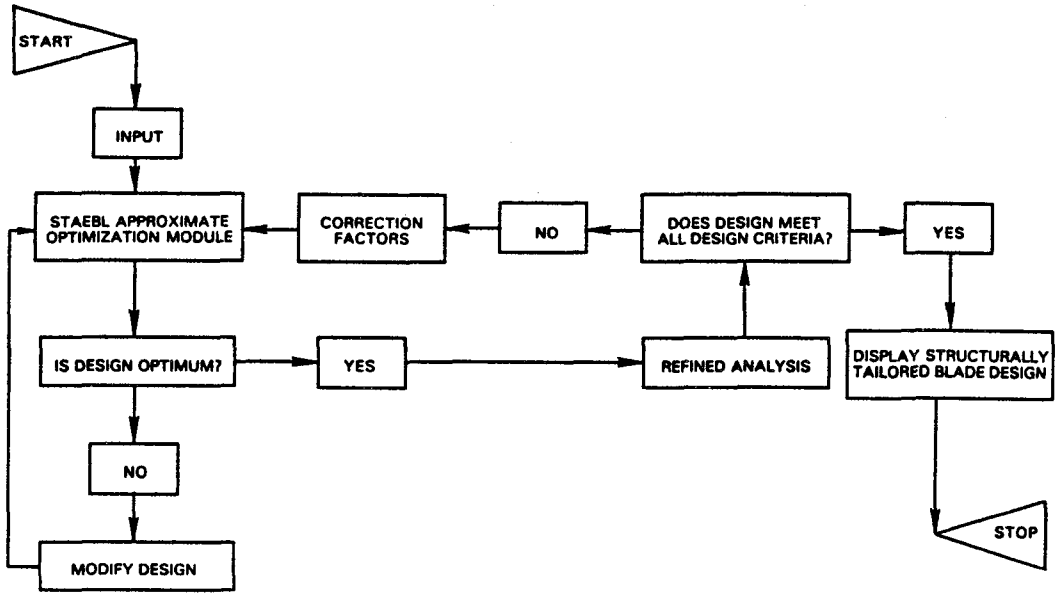

Figure 1 Flowchart for the STAEBL Optimization Process

SECTION 2.0

APPROXIMATE ANALYSES

Due to the number of design iterations required to achieve an optimum blade configuration, many blade analyses must be performed. To derive candidate optima as efficiently as possible, blade optimizations are performed using approximate analysis procedures. These approximate procedures are efficient, fast running, and reasonably accurate. Once a candidate optimum has been achieved, the results of the approximate analyses are checked using more complex, refined analysis. Should the approximate and refined analyses agree within a prescribed tolerance, the design is a valid optimum. Should they disagree, the approximate analysis must be recalibrated, and the optimization process must be reinitiated. It is possible that the refined and the approximate analysis would not show increased agreement even after recalibration. This would mean that the approximate analysis was neglecting an important design parameter, and, as such, should be improved or replaced.

The initial STAEBL program utilized composite beam analysis for the approximate analysis procedure, and NASTRAN plate finite element analysis as the refined structural analysis. Validations of STAEBL yielded optimum configurations for fan blades of hollow and superhybrid construction. When these optimum configurations were evaluated using the refined analyses, the superhybrid blade was shown to be a valid optimum. For the hollow blade, frequency convergence problems were noted, due to chordwise motions inherent to this wide chord, hollow blade. To properly model these complex blades, then, a plate analysis is required.

Using NASTRAN plate finite element analysis, it was demonstrated that relatively coarse meshes could give enhanced approximate analysis results at run times competitive with the original beam analysis procedure. Because the STAEBL approximate analysis must be self-contained, NASTRAN was not a viable approximate analysis option. Hence, a self-contained finite element analysis using NASTRAN plate technology was constructed.

To enable the application of plate finite element technology to STAEBL approximate analysis, an efficient plate finite element procedure was created. The procedure uses NASTRAN technology, but because of its reduced scale, all matrices are stored in core, and all procedures take place in core. Thus, for the small problems of the STAEBL approximate analyses, the special finite element code is able to deliver NASTRAN accuracy, but at greatly reduced computer expense. In fact, for most analyses, the plate technology has proven to be more computer efficient than the previous composite beam approximate analysis procedure.

2.1 Finite Element Analysis

Incorporation of finite element procedures for STAEBL approximate analysis required employing the most efficient solution procedures available. NASTRAN finite element technology was selected for use as the approximate analysis for several reasons:

1. proven computational efficiency,
2. established successful correlations with test experience,
3. convenient input/output, and
4. compatibility with NASTRAN refined analysis procedures.

The use of relatively coarse meshes coupled with Guyan reduction was investigated for analysis applicability. Table I shows a flat plate frequency comparison using the NASTRAN code. The 420 degree-of-freedom model, Guyan reduced to 36 degrees-of-freedom, gave very good frequency correlations relative to refined analysis, but consumed only 9.6 seconds of IBM 3081 computer time.

Table I

Prismatic Cantilever Convergence Study with Guyan Reduction

Initial Degrees-of-Freedom	Degrees-of-Freedom After Reduction	NASTRAN CPU Time, Seconds	Deviation from 900 Degree-of-Freedom Model Frequencies, %		
			First Bending	First Torsion	Second Bending
900	84	24.5	0.0	0.0	0.0
900	45	18.9	0.0	0.2	0.2
420	36	9.6	-0.2	-1.2	-0.8

The efficient plate finite element analysis is fashioned after NASTRAN, using NASTRAN bulk data for its input, and producing NASTRAN displacement and stress output. Thus, identical data pre and postprocessing could be used for the approximate and the refined analyses. Unlike the NASTRAN program, however, all storage and processing is performed in core. This results in a limited capacity for the program, but allowable size is sufficient for STAEBL approximate analyses. In-core processing results in a significant CPU (central processing unit) savings over NASTRAN; the third example of Table I, which ran for 9.6 seconds in NASTRAN, gave identical frequency results in the dedicated finite

element in 3.6 seconds of computer time. Thus, the new code shows a savings of more than 60 percent over NASTRAN for STAEBL approximate analysis. The final Guyan reduction pattern, shown on a fan blade model on Figure 2, reduced a 330 degree-of-freedom model down to 24 degrees-of-freedom and gave frequency results within 1.5 percent of the refined model in 2.3 seconds of computer time.

The A-set pattern was chosen to give maximum accuracy with economical run times. Over the lower 50% of the blade, vibratory motions are primarily in the blade normal direction. Hence, only this degree of freedom was required to be kept in the analysis set. Near the blade tip, due to pretwist effects, motions occur in both the normal and the tangential directions. To properly account for the kinetic energies of these motions, both normal and tangential motions are included on these A-set nodes. To properly prestress the rotating blade, some radial inertias must be included within the A-set. This is accomplished by including the radial motions of the nodes near the blade tip.

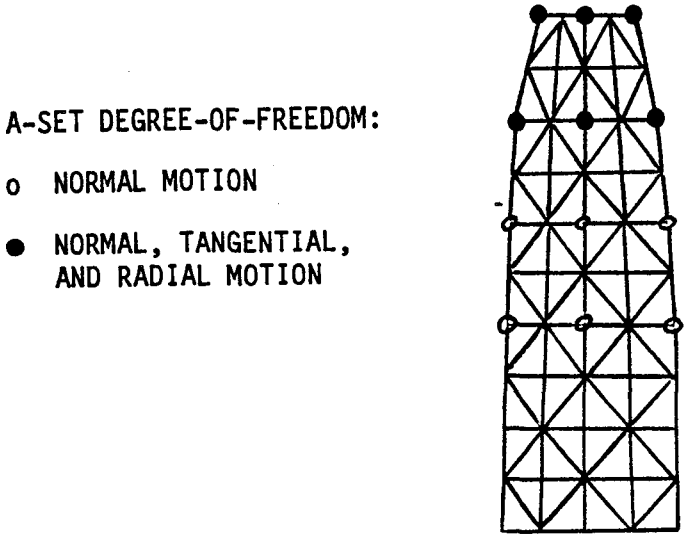

Figure 2 STAEBL Approximate Analysis Guyan Reduction Pattern

2.1.1 The Plate Element

The similarity with NASTRAN was preserved through the usage of a plate bending triangle very similar to the NASTRAN TRIA3 element. The TRIA3 element is a reduced integration triangular plate bending element of the QUAD4 family (Reference 1).

Features of the element include:

1. recognition of thickness taper,
2. properly stacked triangular plate element meshes to simulate airfoil pretwist and camber,
3. composite material capabilities (using lamination theory),
4. element differential stiffness, and
5. lumped masses are employed, assuring a diagonal mass matrix, for storage efficiency.

(Pertinent subroutine: ETR3D)

2.1.2 Guyan Reduction

The Guyan reduction procedure (Reference 2) has proven to be a very successful means of reducing the number of degrees-of-freedom used in dynamic analysis with minimal accuracy loss. The procedure is based on the fact that many fewer grid points are needed to describe the inertia of a structure than are required to describe its stiffness with comparable accuracy. The reduction procedure thus allows a condensation, resulting in a much smaller equation set for dynamic analysis.

The reduced, or omitted, degrees-of-freedom, U_o, and the remaining, or analysis, degrees-of-freedom, U_a, relate to static loads according to:

$$\begin{bmatrix} K_{aa} & K_{ao} \\ K_{oa} & K_{oo} \end{bmatrix} \begin{Bmatrix} U_a \\ U_o \end{Bmatrix} = \begin{Bmatrix} F_a \\ F_o \end{Bmatrix} \tag{1}$$

Neglecting the forces F_o, we find:

$$[U_o] = [G_{oa}]\,[U_a] \tag{2}$$

where

$$[G_{oa}] = -[K_{oo}]^{-1}\,[K_{oa}] \tag{3}$$

The matrix decomposition required to calculate $[G_{oa}]$ in Equation (2) was accomplished by using the LEQ1PB subroutine of the International Mathematics and Statistics Library (IMSL).

The reduced stiffness matrix thus becomes:

$$[\bar{K}_{aa}] = [K_{aa}] + [K_{ao}]\,[G_{oa}] \tag{4}$$

The reduced mass matrix, determined by equating the kinetic energies before and after the reduction, becomes:

$$[M_{\bar{a}\bar{a}}] = [M_{aa}] + [M_{ao}]\,[G_{oa}] + [G_{oa}]^T\,(M_{oa} + M_{oo}\,G_{oa}) \tag{5}$$

(Pertinent subroutine: MNU808)

2.1.3 Differential Stiffness

The determination of natural frequencies for rotating blades requires the inclusion of differential stiffness effects due to centrifugally induced stresses. In order to allow for differential stiffness generation, static deflections are determined for the case of centrifugal loadings, using the LEQT1P solver of the IMSL package. The static displacements are then used to create the element differential stiffness matrix, K_{DGG}. The energy of differential stiffness, U_D, consists of a part, U_{DB}, due to bending motions, and a part, U_{DM}, due to in-plane (membrane) motions:

$$U_D = U_{DB} + U_{DM} \tag{6}$$

As shown in Reference 3, the bending and membrane energies are related to the membrane stresses and the bending rotations, giving:

$$U_D = \frac{hA}{2}\left\{\bar{\sigma}_x\omega_y^2 + \bar{\sigma}_y\omega_x^2 - 2\bar{\tau}_{xy}\omega_x\omega_y + \bar{\sigma}_x(\omega_z^2 + 2\omega_z\epsilon_{xy})\right.$$
$$\left. + \bar{\sigma}_y\,(\omega_z^2 - 2\omega_z\epsilon_{xy}) + 2\bar{\tau}_{xy}\,(\epsilon_y - \epsilon_x)\,\omega_z\right\} \tag{7}$$

where hA is the element volume, $\bar{\sigma}_x$, $\bar{\sigma}_y$ and $\bar{\tau}_{xy}$ are the element membrane stresses, and ω_x, ω_y and ω_z are the rotations in the element coordinate system, shown on Figure 3.

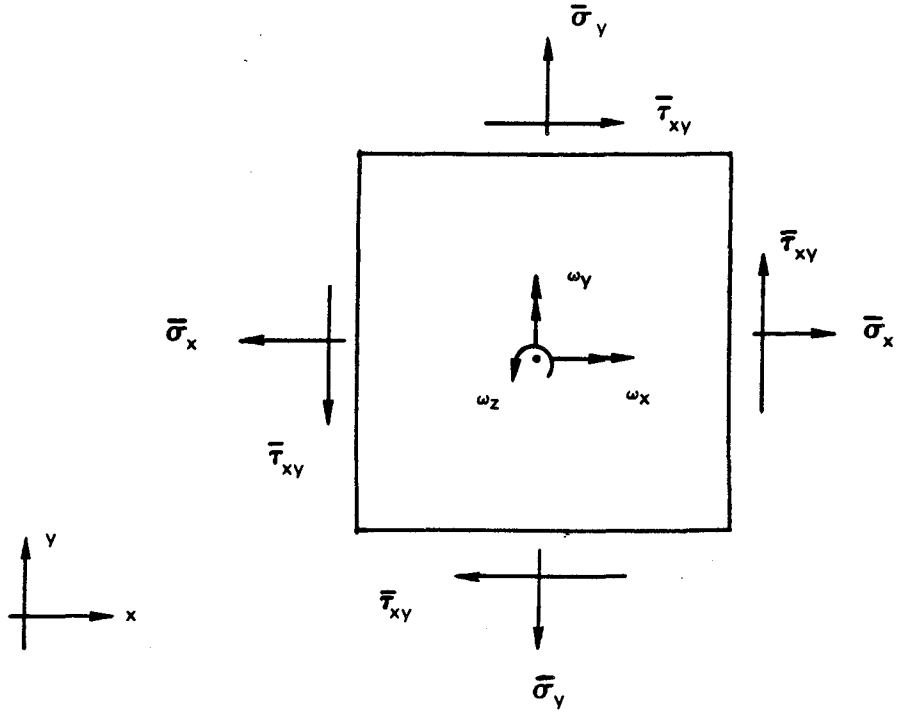

Figure 3 Stresses and Rotations of Prestress Stiffened Plate Element

The centrifugal mass matrix, which accounts for the change in direction of centrifugal loads with displacement, gives the nodal incremental load in global coordinates (x = radial, z = axial), as:

$$\begin{Bmatrix} \Delta F_x \\ \Delta F_y \\ \Delta F_z \end{Bmatrix} = - \begin{bmatrix} m\Omega^2 & 0 & 0 \\ 0 & m\Omega^2 & 0 \\ 0 & 0 & 0 \end{bmatrix} \begin{Bmatrix} \Delta X \\ \Delta Y \\ \Delta Z \end{Bmatrix} \qquad (8)$$

The "stiffness", transformed into local nodal coordinates, is combined with the differential stiffness matrix and the original blade stiffness, to give the blade's total at-speed stiffness.

The total blade stiffness matrix, after reduction to analysis-set size, is solved to find the at-speed blade frequencies.

(Pertinent subroutines: MNU808, CTMASS)

2.1.4 Eigenvalue Solution

Once the stiffness and mass matrices have been reduced, they are, in general, symmetric but full. Due to the reduction procedure, however, they are relatively small in size. The unsymmetric eigenvalue problem becomes:

$$-\omega^2\{u_a\} + [M_{aa}]^{-1}\,[K_{aa}]\,\{U_a\} = \{0\} \tag{9}$$

The IMSL package was again employed, using the QR method to solve the unsymmetric eigenvalue problem. Both eigenvalues and eigenvectors are extracted for the reduced size problem. IMSL routines required to perform the eigenvalue extraction include: EBALF, EHESSF, EHBCKF, EQRH3F, and EBBCKF.

2.1.5 Eigenvalue Speed Sensitivity

Fan blades must operate over a range of engine speeds. The variation of frequency with speed, shown on Figure 4, may be nearly expressed as:

$$f^2 = fo^2 + BN^2, \tag{10}$$

where fo is the zero speed frequency, and N is the engine RPM. To evaluate the modal speed sensitivity coefficient, B, frequencies at two discrete speeds must be determined. If both speeds are selected from the engine running range, the frequency estimate will be quite close over the entire running range.

The stiffness matrix at the second speed may be determined without a stiffness recalculation by scaling the differential stiffness matrix with the square of the speed ratio. A second eigenvalue solution is performed, but, for economy, no eigenvector extraction is performed - mode shapes from the first analysis speed are saved for delivery to downstream modules. Thus, the first analysis speed must correspond to the flutter conditions to be analyzed - typically the engine redline speed.

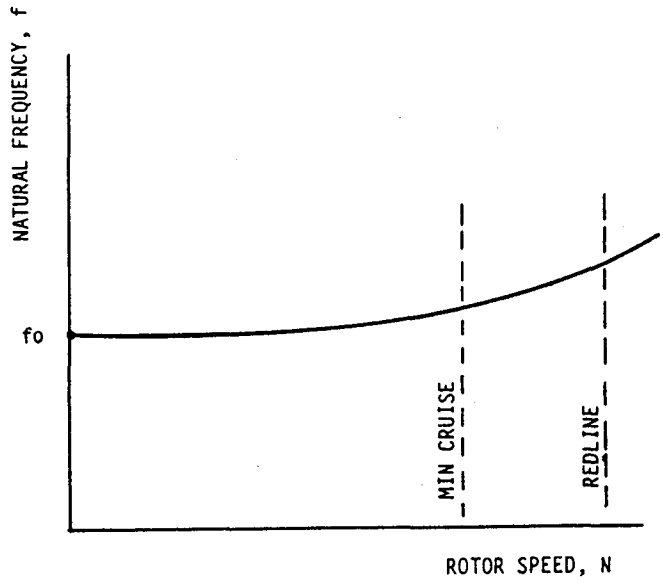

Figure 4 Blade Natural Frequencies Increase With Speed

(Pertinent subroutine: MNU808)

2.1.6 Finite Element Mesh Generation

Due to the high number of approximate finite element analyses performed by the STAEBL system, efficient mesh generation is important. Additionally, mesh generation accuracy aids refined analysis recalibration, and provides proper gradient information for the optimization scheme.

The basic blade description of STAEBL is an x-y coordinate description of each cross section exterior. As shown by Figure 5, the section chord line defines the local x axis. Blade stagger angles, α, define the angular section orientations. Cross sections are radially stacked by center of gravity.

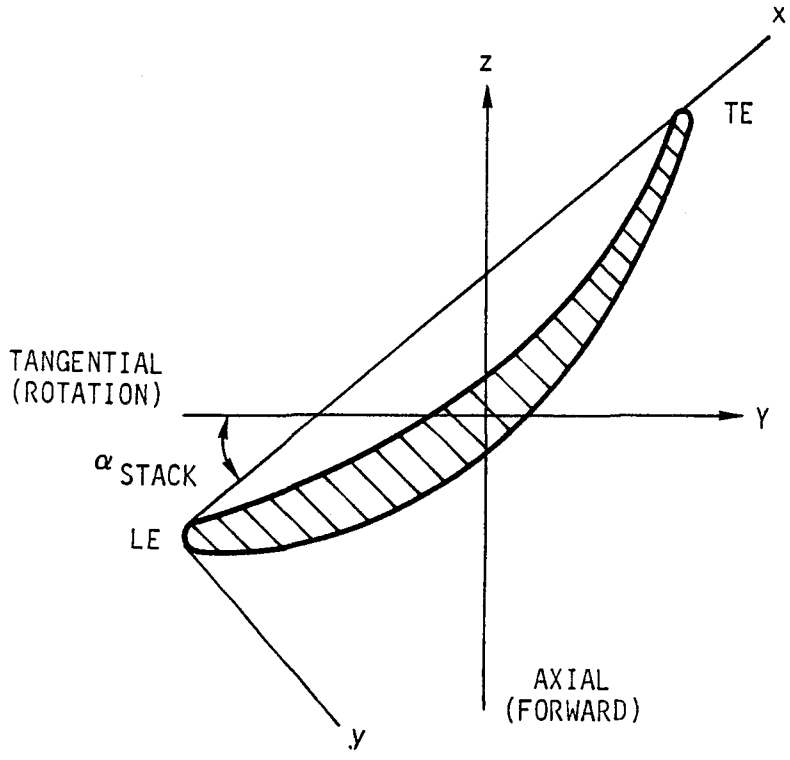

Figure 5 STAEBL Cross Section Coordinate Definition

Blade design perturbations are developed by scaling the above basic coordinate description. If the section chord is altered, all local x coordinates are scaled in proportion to the relative chordal variation. If the section maximum thickness is perturbed, local y coordinates are scaled to describe the new thickness. Leading and trailing edge radii are unperturbed. Thus, thickness scaling is a function of the local x value, with 100 percent of the thickness variation occurring at the maximum thickness point, and with the thickness variation linearly scaled to no change at the leading and trailing edges.

Airfoil mesh generation requires the generation of section coordinates at airfoil radial grid point locations. This is done by interpolation of the scaled blade coordinates to generate coordinates at the required spanwise locations. Mean line section coordinates are generated from the scaled section coordinates. At appropriate chordwise locations, blade thickness is determined. Mean line coordinates, which define the finite element grid point locations, are translated and rotated about the blade stacking line to transform the nodal coordinates into the engine coordinate system, where the x axis is a radial stacking line, and the z axis is the engine axis, positive rearward.

In the area of the blade attachment and extended neck modeling, special treatment is required to generate coarse models of blades of conventional, straight root design. The first row of nodes for a model conventional root blade is generated to fall on a straight line, oriented at the proper dovetail broach angle. The first element row, which represents the blade neck, has a constant thickness equal to the nominal neck thickness. The second row of airfoil nodes, which represents the top of the neck and the airfoil root, is located to represent the airfoil geometry, including the conical flow path orientation of the platform, as shown on Figure 6. Thus, in its present form, STAEBL makes an approximation of the neck geometry. Due to the lack of rigid body elements, the block neck elements have camber at the platform, unlike a conventional neck which is a parallelogram in cross-section. This modeling approximation will be improved in the next version of STAEBL. For composite blades, no blade neck section is generated. Instead, the neck is treated as an extension of the airfoil. This curved root concept with a separate platform is a good representation of a typical composite blade.

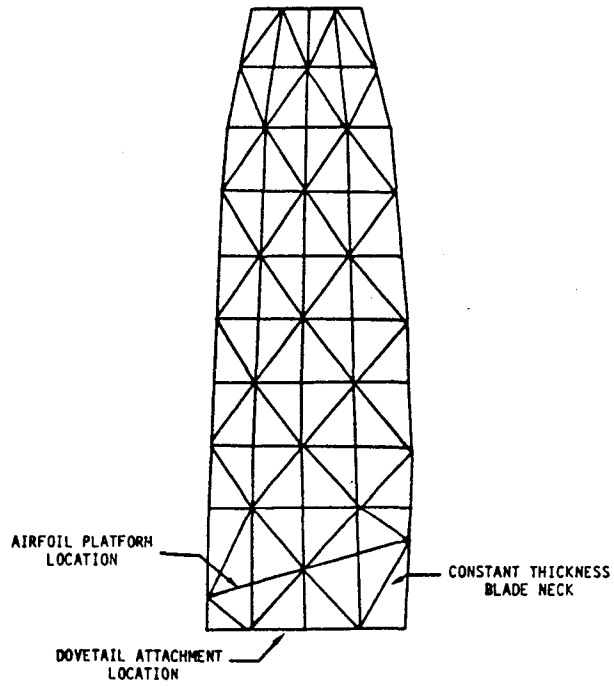

Figure 6 STAEBL Blade Neck and Attachment Models

Equivalent properties for composite materials are generated in the mesh preprocessor, by applying lamination theory to the composite blade construction, while maintaining the blade aerodynamic profile. For the superhybrid blade, the first materials accounted for are the titanium skins and center ply. Any remaining material is filled with boron/aluminum and graphite/epoxy in a selected volume fraction, with the graphite inside the boron plies. The layup is considered to be symmetric, so that no coupling exists between the bending and membrane stiffness. Application of lamination theory (Reference 4) to the composite element yields effective stiffness arrays for membrane and for bending motions. These matrices are compatible with NASTRAN material descriptions for the plate elements employed.

When processing a hollow blade, the location of the hollow and treatment of its movement requires care to ensure that STAEBL will be able to evaluate meaningful design variable gradients. Due to the high degree of flexibility allowed to hollow movement, it is not practical to move the nodal mesh with the hollow - very badly shaped elements could result, which would degrade the accuracy of the approximate analysis. Rather, the element locations are constant, and the hollow moves relative to those elements. If an element is fully penetrated by the hollow, the hollow is treated as a zero stiffness, zero mass lamina, and the equivalent material properties are calculated using standard lamination theory. If an element is only partially penetrated by the hollow, the hollow thickness is scaled down by the areal penetration ratio, and the entire element is considered to be hollow, with a reduced hollow thickness. This prevents possible on/off discontinuities from occurring, and ensures continuous derivatives for the design sensitivity calculations.

User alterations to the mesh to be generated can be accomplished through FORTRAN updates, although increases in mesh complexity must be accompanied by increased storage capabilities for the finite element code. Changes to the generated finite element mesh may be made by altering the NPS (number of chordwise nodes) and NSPAN (number of radial nodes) parameters within SUBROUTINE STAEBL. Currently, these values are 5 and 11 for STAEBL blade analysis, and 5 and 7 for local FOD analysis. Changes to the generated A-set pattern may be accomplished through updates to SUBROUTINE BC, which defines RFORCE, SPC, and ASET cards.

(Pertinent subroutine: STAEBL)

2.1.7 In-Plane Rotation Singularity Constraint

When performing plate finite element analysis, the in-plane rotations must be suppressed in relatively flat sections to prevent system ill-conditioning. On airfoils, camber is usually sufficient near the blade root to prevent in-plane rotation singularities. Near the blade tip, however, camber is low and suppressions are usually required.

An automated rotation singularity constraint processor was incorporated within the STAEBL mesh generator. Local nodal displacement coordinate systems ensure that the local y axis is normal to the airfoil mean line. Nodal in-plane rotation constraints are generated when the angle between adjacent node-to-node secants of a cross-section is 5° or less, as shown on Figure 7. Leading and trailing edge in-plane rotations are automatically constrained due to the relative straightness of the blade edges.

(Pertinent subroutine: STAEBL)

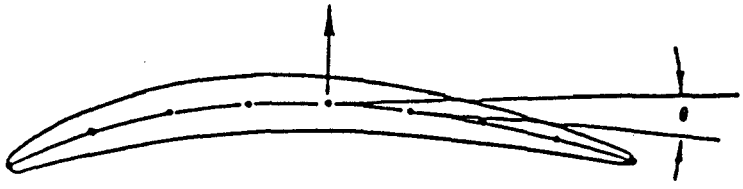

Figure 7 Cross Section Secant Angles are Checked for In-Plane Rotation Constraint Generation

2.1.8 Postprocessing of Finite Element Output

Static stresses and at-speed eigenvalues, eigenvectors, and nodal stresses are all output from the finite element code. Many of these data must be post-processed before they may be used either for constraint evaluation or as input to other subroutines. Element stresses must be converted into ply stresses for both static and dynamic modes at elements of stress interest. Additionally, the flutter analyses require both frequency and mode shape information.

The evaluation of static and vibratory composite blade ply stress values requires processing of the element stress values based upon the application of lamination theory (Reference 4). The lamination theory assumes that plane sections (through the plate thickness) remain plane after deformation. The laminate processor provides the matrices required to convert element stresses to element membrane and bending strains. Then, based on the lamination assumptions, ply strains are calculated, leading to ply stresses, and, ultimately, to the TSAI-WU tensor failure theory equivalent stress evaluation (Reference 5).

The evaluation of flutter constraints requires that equivalent beam mode shapes be generated from the available plate mode shape data, due to the beam theory of the present flutter codes. Beam mode shapes are generated from the available plate mode shapes by performing a spline fit of each component of the mode shape on each cross section. From the spline fit, modal bending and torsional motions are determined at the section shear center, for transmittal to the flutter analysis.

(Pertinent subroutines: STRES2, TSAIWU)

2.2 Local Foreign Object Damage Analysis

An approximate foreign object damage analysis model has been developed that is computationally efficient and preserves the major interactions of the foreign object impact event. The analysis generates incremental loads from user-defined projectile data. The dynamic impact event is simulated through modal transient integration of a linearized target model. Mode shapes used in this process are provided by STAEBL's finite element analysis, incorporating elements specially modified for the foreign object damage analysis. A maximum average airfoil leading edge strain is then calculated and used in the blade optimization process. The analysis flow is shown in Figure 8.

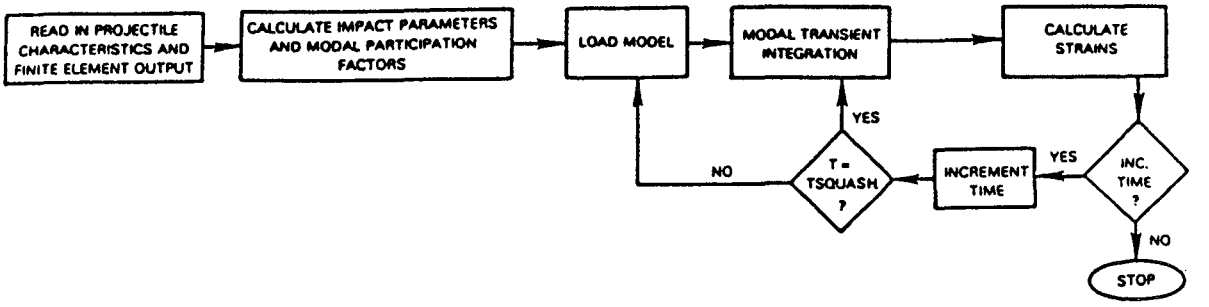

Figure 8 Flowchart of Foreign Object Damage Analysis

2.2.1 Load Approximation

Foreign Object Representation

Several characteristics of the impact event had to be considered in developing an accurate but efficient load model. The load model has to duplicate the physical aspects of the foreign object. The analysis assumes a spherical projectile body (for which there is published test data) which is normally given a density of 0.0325 lb/in^3 (a density 90 percent of water) and a mass of 1.5 lb (a typical Federal Aviation Administration requirement). The user must also define the impact velocity and angle (these are functions of aircraft velocity, engine speed, impact radius and the blade stagger angle) and the projectile slice height (normally the worst condition is considered). These values are important in accurately representing the projectile.

(Pertinent subroutine: PROJ)

Target Loading

An accurate representation of projectile loads must account for the interactions between the projectile and the target during the impact event. The impacted footprint, as well as spatial and temporal load variations, have significant effects on the deflected shape.

To aid in the development of the simplified load model, a refined load model using fluid finite elements was built to simulate the impact event. Based upon transient finite element analysis using the fluid model, it was found that, for a rigid target:

a. nodal points located within one bird diameter of the impact center point were subjected to impact loading;

b. load duration was equal to the bird squash-up or

$$Tsquash = 2 * R / VP$$

where R = projectile radius, and
VP = projectile velocity;

c. the maximum load for any given node could be approximated by assuming a parabolic load distribution between the impact center and edges:

$$FAMPY = (FAVEY/SUM) * AA1 * AA2$$

where FAVEY = average total force applied to the nodes for a rigid target = projectile normal momentum / Tsquash,
SUM = sum of correction factors AA1 and AA2,
AA1 = 1 - Y/R
= linear adjustment for axial node distance from the (fixed) center of impact, and
AA2 = $1 - X^2/(4R^2)$
= parabolic adjustment for radial node distance from the center of impact.

Thus, loads are distributed as shown in Figure 9:

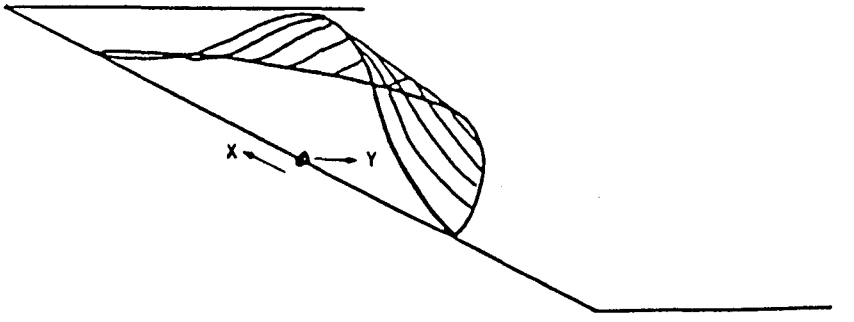

Figure 9 Approximated Load Distribution Using Parabolic Adjustment

d. nodal loading (constant with time) could be assumed to be such that the sum of impulses was equal to the projectile slice momentum normal to the surface of the target.

It was found that for the simplified load model, maximum loads could, with reasonable accuracy, be assumed to act initially over the leading edge of the target. Investigations of the refined fluid model results have also shown that downstream nodes lag the upstream nodes according to the time required for the projectile to reach them. Thus, as the event progresses, more nodes become loaded. Once the projectile slice normal momentum has been applied to the target impact area, all loads are removed. The approximate model loading is defined such that:

FAMPY = 0 if TIMEA is less than TSTART

= 0 if TIMEA is greater than TSQUASH

= calculated maximum loading for that node

where TIMEA = time since initial target impact, and

TSTART = nodal loading start time defined by nodal chordwise distance from the target leading edge divided by the projectile velocity.

(Pertinent subroutine: LOAD)

Target Compliance

By plotting the load history of various nodes, impact loads were shown to be dependent upon target compliance (Figure 10).

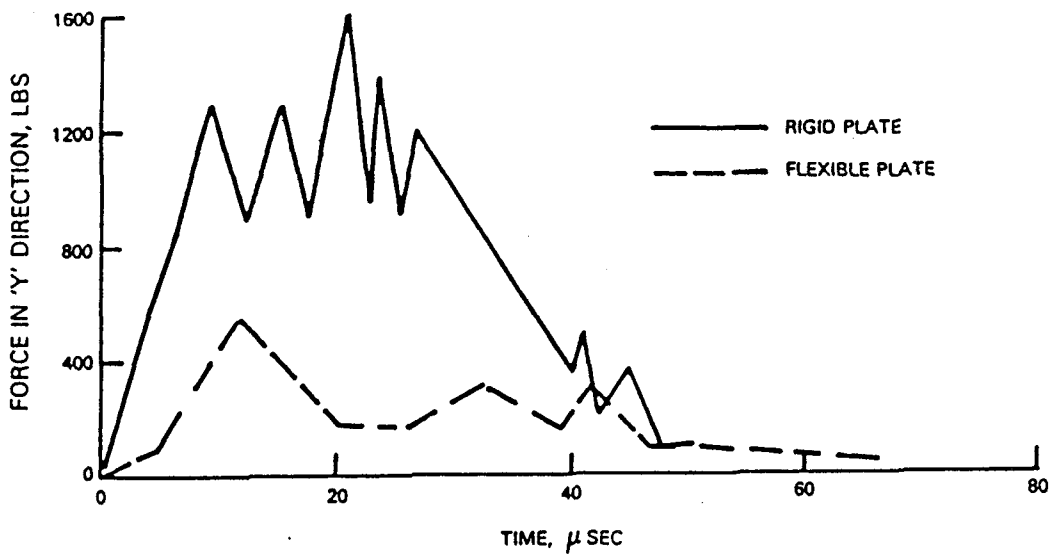

Figure 10 Dependence of Impact Loads on Target Compliance

This necessitated the further development of the approximate load model to be based upon momentum transfer principles, where interaction between the projectile and the target influenced the forces applied to the model. Nodal forces are determined using the relative velocity between the projectile and the deflecting target. The maximum node force FAMPY is adjusted downward to account for relative motion of the projectile and target:

$$FEXT = FAMPY * VELRAY$$

where VELRAY is the ratio of relative velocity to projectile normal velocity.

Target flexibility reduces the instantaneous projectile loads by reducing the relative velocity between projectile and target. However, deflection of the target also changes the relative positioning of projectile and target. Therefore, extra material is ingested and there is an increase in the total momentum exchange, as shown in Figure 11.

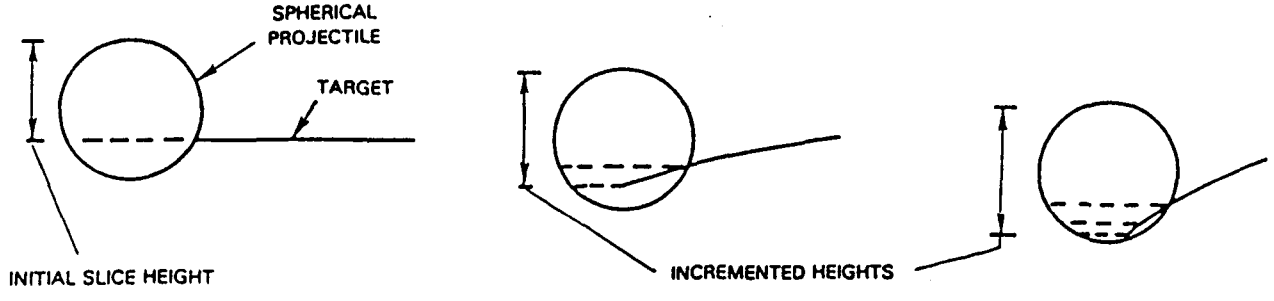

Figure 11 Effect of Target Deflection on Material Ingested

As the target begins to deflect, the leading edge cuts the spherical projectile at a greater distance from the mass center. As edge deflections continue and the ingested mass increases, the total impulse on the target due to the projectile is incremented. This is called the "extra slice" calculation and is performed by calculating the increased volume of the projectile forward of the target's leading (cutting) edge, as shown in Figure 12.

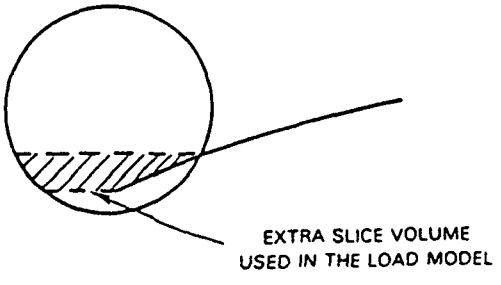

Figure 12 Projectile Volume Used in the "Extra Slice" Calculation

The node force FEXT is then adjusted as follows:

$$FEXT = FEXT * (1 + ESLICE/BIM)$$

where ESLICE = mass of the extra slice, and
BIM = initial projectile (bird) impact mass.

Thus, while no extra nodes are loaded, the momentum increment due to target flexibility is properly accounted for.

The parabolic node loading coupled with the extra slice calculation has shown good load comparisons with nonlinear finite element results.

2.2.2 Finite Element Model

The large deflection, nonlinear structure is treated as a fully yielded, moderate deflection system. This results in a linearized model from which natural vibration modes may be obtained. The responses of these natural modes are then determined using modal transient analysis.

The selection of the area of blade to be modeled for the impact event and the large, nonlinear deflection (normally associated with foreign object damage) required careful consideration.

Local Patch

It has been shown (both through field experience and refined analysis) that foreign object damage caused by bird ingestion is, in the case of fan blades, most severe in the outer 50 percent of the blade. This is where velocity is relatively high and the critical airfoil thicknesses are at a minimum. This is especially true for the leading edge, where foreign object damage occurs. In addition, it has been shown that if a strike occurs at 70 percent span, the blade tip is hardly affected. It is for these reasons that a "local patch" model of the impact zone is used (Figure 13).

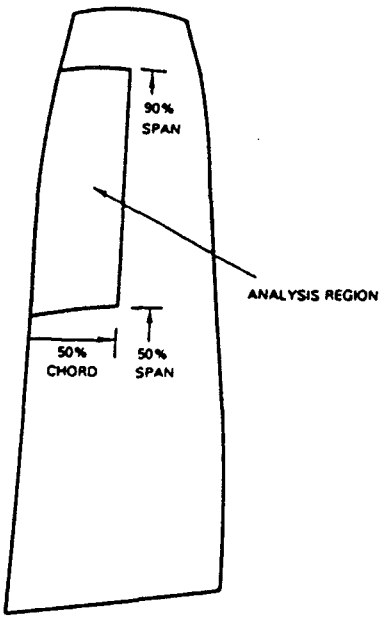

Figure 13 "Local Patch" Model

The local patch model is made from the coordinate data of the candidate airfoil, running from 50 percent to 90 percent span and 0 percent to 50 percent chord. Projectile impact is assumed to occur at 70 percent span (impact near the tip is not as likely to fail the blade).

Large-Scale Deflection

Large-scale deflections usually accompany the impact event, and in a large percent of the loaded impact zone, the blade material has strained well beyond yield in the radial direction. Nonlinear analysis of plate specimens has shown that stresses beyond yield can be assumed to be essentially constant, as illustrated in Figure 14.

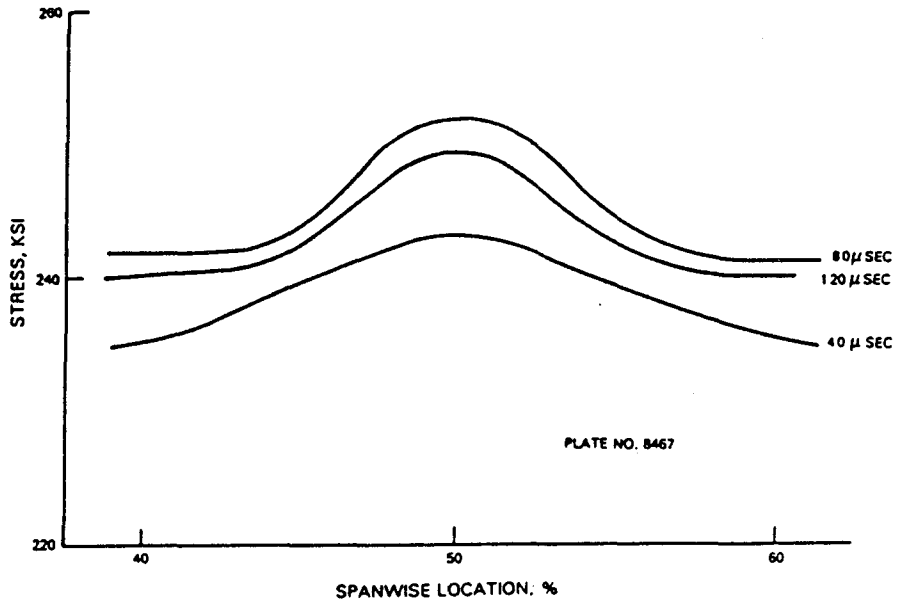

Figure 14 Stress Histories of Large Deflection Model (Plate No. 8467)

Validity of the fully stressed leading edge assumption was demonstrated by examining stress and strain histories from a large deflection model of a flat plate severely impacted by a gelatin ball (Figure 14). The spanwise stresses are nearly constant along the leading edge as the impact progresses through time for spanwise positions near the impact location. The leading edge stresses are almost purely membrane. Concave and convex stresses are nearly equal, indicating an almost purely membrane condition. Figure 15 shows the chordwise stresses along the impact centerline. With the exception of the extreme leading edge where Poisson effects predominate, the stress is mostly bending in nature, with relatively little yield even with this very severe impact.

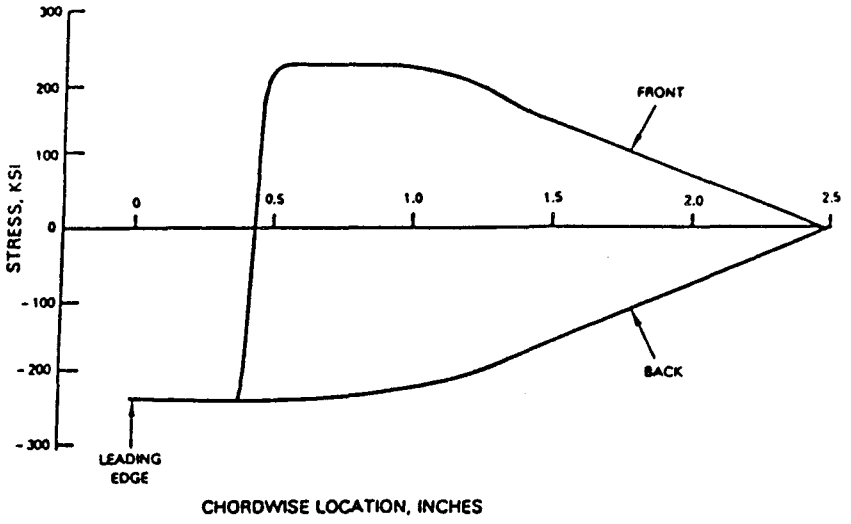

Figure 15 Chordwise Stresses Along the Impact Centerline

These phenomena are incorporated into the leading edge elements of the local patch model and allow for the simulation of large, nonlinear deflections associated with foreign object damage. This is accomplished by modifying the membrane stiffness in the radial direction (to reflect a fully yielded condition) and zeroing-out the spanwise bending stiffness. For an 8 x 12 element breakup (like that used in the local patch model), the special elements are placed as shown in Figure 16.

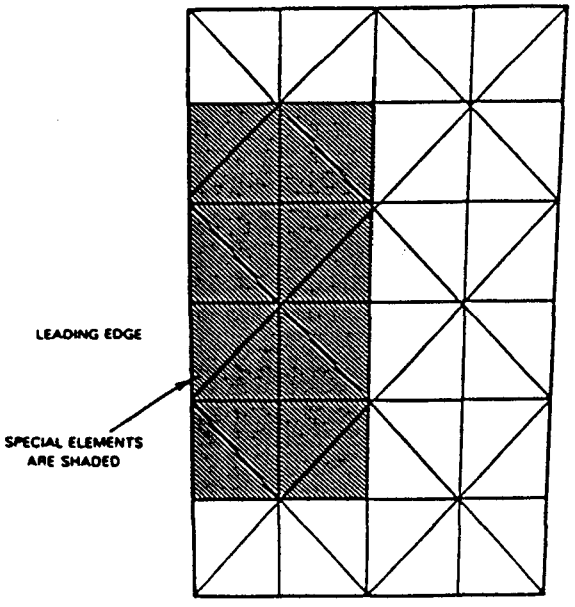

Figure 16 Placement of Special Elements Using an 8 x 12 Element Breakup

2.2.3 Revised Element Stiffness

The STAEBL finite elements are oriented so that the element x-axis is in the blade radial direction, as shown on Figure 17. For the large deflection, fully yielded element, we will consider one degree-of-freedom per node - the out-of-plane displacement, w. The radial stress is fully yielded (perfectly plastic), so that:

$$\sigma_x = \sigma_{yield} \tag{11}$$

The element strain energy, then, is $U = \int_V \sigma_x \epsilon_x dV$.

The radial strain, ϵ_x, may be determined by applying a distance calculation to side 1-2, as:

$$\epsilon_x = \frac{\sqrt{(w_2 - w_1)^2 + x_2^2} - x_2}{x_2} = -1 + \sqrt{1 + \left(\frac{w_2 - w_1}{x_2}\right)^2} \tag{12}$$

Assuming moderate deflections, we are able to take a two-term polynomial expansion for the term under the square root, as:

$$\sqrt{1 + a^2} \approx 1 + \frac{1}{2} a^2 \tag{13}$$

The strain thus becomes:

$$\epsilon_x = \frac{1}{2}\left(\frac{w_2 - w_1}{x_2}\right)^2 \tag{14}$$

The radial stress and the radial strain, being constant, may be removed from the strain energy integrand, leaving $\int_V dV = 1/2\ x_2 y_3 t$ for the volume integral. The strain energy, in matrix form, thus becomes:

$$U = \frac{y_3\ \sigma_{yield} t}{4\ x_2} \begin{Bmatrix} W1 \\ W2 \\ W3 \end{Bmatrix}^T \begin{bmatrix} 1 & -1 & 0 \\ -1 & 1 & 0 \\ 0 & 0 & 0 \end{bmatrix} \begin{Bmatrix} W1 \\ W2 \\ W3 \end{Bmatrix} \tag{15}$$

Minimizing the strain energy with regard to the three displacements gives the element stiffness matrix,

$$[K] = \frac{y_3}{2x_2}\ \sigma_{yield}\ t \begin{bmatrix} 1 & -1 & 0 \\ -1 & 1 & 0 \\ 0 & 0 & 0 \end{bmatrix} \tag{16}$$

The terms of this stiffness matrix replace the spanwise bending stiffnesses of the linear, elastic triangle. The zero stiffness on the third node is not of concern, for the other element of the triangle pair will provide the appropriate stiffness to this node.

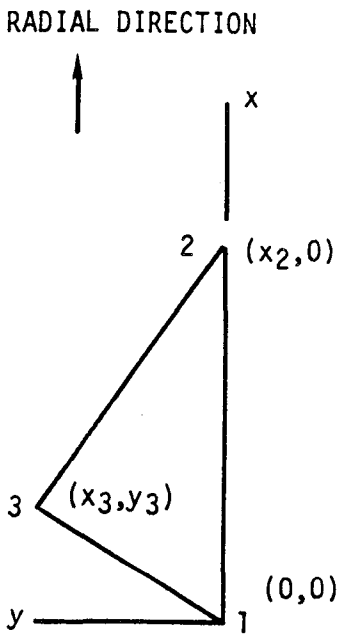

Figure 17 STAEBL Element Local Coordinate System

The membrane effect can be observed by comparing the frequencies generated by a finite element analysis of the local patch model with and without the large displacement correction. The fundamental mode with element modifications is significantly higher in frequency. For one particular plate, frequencies were as follows:

Mode	Model With Normal Elements (HZ)	Model With Modified Elements (HZ)	Comments
1	2402	5375	Fundamental leading edge spanwise mode.
2	6724	5958	Chordwise modes. Note the frequency decrease in most of these modes due to the loss of radial bending stiffness.
3	7871	6682	
4	12099	11978	
5	13475	13640	

The membrane generalization of the elements within the impact region provides a good approximate simulation of the large, inelastic deflection that occurs during the impact event.

(Pertinent subroutine: ETRFOD)

2.2.4 Modal Transient Analysis

The local patch vibration modes are then passed to the transient integration analysis. Modal transient integration provides the target response to the projectile loading and, since projectile loading is a function of target deflection, allows the loading model to interact with the modal structural model.

General

Modal analysis is based on the principle that any statically deformed element can be described by a combination of that element's mode shapes. Once the coefficient of each mode's participation is calculated, the impact event can be simulated by the integration of a series of linear steps through time. The deflected shape due to impact is rather basic; therefore, only the first five modes of the patch model are required. The entire calculation proceeds very quickly, due to the uncoupled nature of the modal responses.

Theory

The basic equations used in the analysis are taken directly from the NASTRAN Theoretical Manual (Section 11.4.1). Very little structural damping occurs during the impact event; therefore, damping is assumed to be zero. With no nonlinear terms present, the modal equations of motion are uncoupled, with each modal coordinate (A_i) satisfying a separate differential equation:

$$M_i \ddot{A}_i + K_i A_i = P_i(t) \tag{16}$$

The general solution to Equation (16), expressed in terms of arbitrary initial conditions, $A_{i,n}$ and $\dot{A}_{i,n}$ at $t = t_n$, and a convolution integral of the applied load is, for $t \geqslant t_n$,

$$A_i(t) = F(t-t_n)\, A_{i,n} + G(t-t_n)\, \dot{A}_{i,n} + \frac{1}{m_i} \int_{t_n}^{t} G(t-T)\, P_i(T)\, dT \tag{17}$$

By assuming a linear load variation between time points, the integral in Equation (17) may be evaluated in closed form. The solutions at the subsequent time point, $t = t_{n+1}$, in terms of the initial conditions at $t = t_n$ and the applied loads is:

$$A_{i,n+1} = FA_{i,n} + G\dot{A}_{i,n} + AP_{i,n} + BP_{i,n+1} \tag{18}$$

$$\dot{A}_{i,n+1} = F^1 A_{i,n} + G^1 \dot{A}_{i,n} + A^1 P_{i,n} + B^1 P_{i,n+1} \tag{19}$$

The coefficients for the recurrent solutions are tabulated in Reference 3. Once the coefficients have been evaluated, the iteration algorithm of Equations (18) and (19) proceeds very quickly.

(Pertinent subroutines: FGAB, MODINT)

2.3 Forced Response and Life Assurance

High frequency fatigue failure is currently prevented by designing blades to avoid natural frequencies which are coincident with strong excitations at high operating power. A forced response model is available in STAEBL as an option to prescribed resonance margins. The forced response option in STAEBL allows the blade resonance requirements to be based on its forced vibration and steady stress characteristics.

2.3.1 General Calculation Flow

When the forced response option has been employed, STAEBL will determine the magnitude of the blade forced response for user-defined excitation orders. Using output from the finite element analysis where frequencies, mode shapes and steady stress values were generated, the location of the worst vibratory and steady stress combination for each mode is determined. Using the appropriate forcing function and a calculated stress per unit force ratio, the acceptability (or life margin) figure is generated. Figure 18 shows the flow of this process.

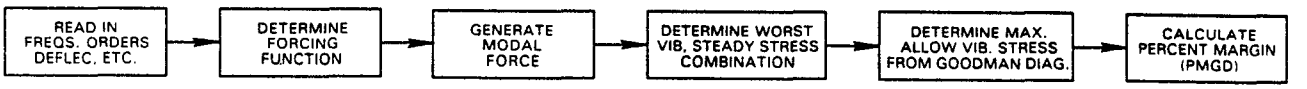

Figure 18 General Calculation Flow

2.3.2 Forced Response Theory

Amplification Ratio

The steady state solution of the second-order differential equation of forced damped harmonic vibration is used to derive the amplification factor for the damped one degree-of-freedom system. The response is shown in Figure 19 (Reference 6).

$$\frac{Xk}{F_0} = \frac{1}{\sqrt{\left[1-\left(\frac{\omega}{\omega_n}\right)^2\right]^2 + \left[2\zeta\left(\frac{\omega}{\omega_n}\right)\right]^2}}$$

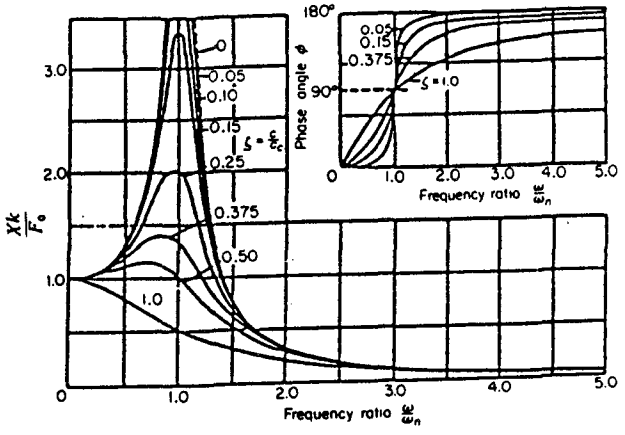

Figure 19 Amplification Factor

Stress during resonance, for a given forcing function, is established by a balance between work done by excitation (which is proportional to amplitude) and work done by damping (which is proportional to amplitude squared). However, in the case of engine blades, where there is normally a 5 or 10 percent margin at the resonance margin of interest, the damping effects are so small that they hardly affect the amplitude ratio:

$$\text{AMP. RATIO (A.R.)} = \frac{1}{\sqrt{\left[1-\left(\frac{1}{FM+1}\right)^2\right]^2 + \left[2\zeta\left(\frac{1}{FM+1}\right)\right]^2}}$$

Frequency Margin, FM	Logarithmic Decrement	Damping Coefficient, ζ	Amplitude Ratio
.05	0.0	0.0	10.756
.05	0.003	0.001	10.756
.05	0.013	0.002	10.747
.05	0.025	0.004	10.720
.05	0.038	0.006	10.676
.05	0.050	0.008	10.614
.05	0.063	0.010	10.537

This is useful in STAEBL because aerodynamic damping, as well as mechanical damping, do not have to be evaluated in establishing, to a first order approximation, the forced response stresses. However, this is not true if the blade frequency is very close to the excitation frequency.

2.3.3 Modal Forced Response

For application to STAEBL, the forced vibration equilibrium Equation (20) was transformed to uncoupled modal form, Equation (21), where Y is the modal coordinate.

$$[M]\{\ddot{x}\} + [K]\{x\} = F \sin(\omega t) \tag{20}$$

$$\underbrace{\{\lambda\}^T[M]\{\lambda\}}_{GM}\ \ddot{Y} + \underbrace{\{\lambda\}^T[K]\{\lambda\}}_{GS}\ Y = \underbrace{\lambda^T\{F\}}_{\text{modal force}} \sin(\omega t) \tag{21}$$

where GM is generalized mass,
GS is generalized stiffness, and
λ is the modal vector.

The modal amplitude to the sinusoidal exciting force may be expressed as:

$$Y = Y_o \frac{1}{1 - \left(\frac{\omega}{\omega_n}\right)^2} \sin \omega t \tag{22}$$

where Y_o is the response of the mode to the statically applied modal force,

$$Y_o = GS^{-1} (\lambda^T) \{F\} \tag{23}$$

The amplitude of vibratory response, then, can be expressed as a multiple of the modal vibratory stress,

$$\sigma_v = Y_o \frac{1}{1 - \left(\frac{\omega}{\omega_n}\right)^2} \sigma_m , \tag{24}$$

where σ_m is the modal stress vector.

2.3.4 Life Fraction

The fatigue life acceptability of the candidate design is evaluated by finding the element of the finite element model with the worst combination of vibratory and steady stresses when plotted on the Modified Goodman Diagram of Figure 20. The ratio of vibratory stress to allowable vibratory stress at the given steady stress, designated as the PMGD (Percent Margin on the Goodman Diagram), is used to measure the severity of the resonant stress.

When a design has a maximum PMGD less than or equal to 1.0, it is deemed to be acceptable, even though the resonance margin may be less than 5 percent. One test case of a highly root stressed blade showed that the resonance margin had to be much larger than 5 percent to guarantee acceptability as defined by the Goodman Diagram procedure. Thus, blades optimized for minimum weight or high steady stress are going to prove quite sensitive to forced response vibratory stresses.

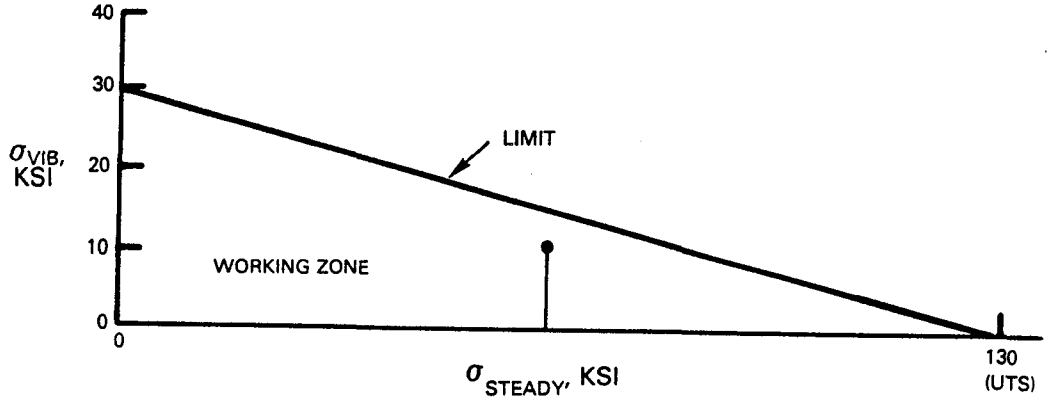

Figure 20 Location of the Worst Vibratory and Steady Stress Combination on the Modified Goodman Diagram - STAEBL

(Pertinent subroutine: GOODMN)

2.3.5 Resonance

STAEBL checks the effect of all user-input forcing functions on the first three modes (unless user-defined forcing functions are supplied for additional modes) at redline and minimum cruise speeds. In addition, STAEBL checks for any resonances that may occur within the operating range. If a resonance is found, the forced response for a resonance condition is evaluated. Here damping is critical, of which the major portion is aerodynamic. For the resonant condition, a value typical of zeta (damping ratio) is used, corresponding to an aerodynamic log decrement of 0.050. In most cases the PMGD factor is greater than 1.0 and STAEBL is forced to move the mode out of the operating range.

2.3.6 Energy Efficient Engine Fan Forcing Functions

The STAEBL forced response algorithm was established based on the concept that the user must supply his own forcing function through SUBROUTINE FRCFNC. For code evaluation purposes, forcing functions have been established for the baseline Energy Efficient Engine hollow fan blade, based on the assumption that resonance margins of less than 5 percent would result in fatigue failure for the hollow fan blade. The selection of 5 percent margin implies that a modal amplification of 10 would be allowed over the modal static response, Y_0. The forcing function was assumed to act at the 25 percent chord location and

to vary linearly from 0 to Fmax in the spanwise direction, as shown in Figure 21. This choice of load functional variation guarantees that both bending and torsional modes will be aerodynamically excited.

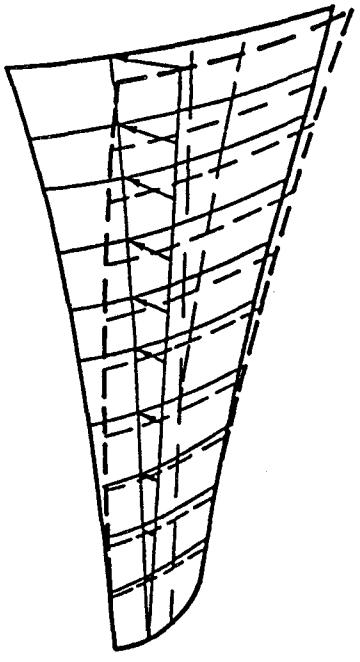

Figure 21 Forcing Function Increasing from the Airfoil Root to Tip

Representing the forcing function as a scalar muliplier, F_m, times F_{unit}, a linear function of blade radial coordinate which is 0 at the root and 1.0 at the tip, we have:

$$F = F_m F_{unit} \tag{25}$$

The static deflection, Y_o, then is:

$$Y_o = (GS)^{-1} \lambda^T F_m F_{unit} \tag{26}$$

For application to the Energy Efficient Engine blade, a 5 percent margin implies an amplification factor of 10, resulting in vibratory stresses at the Goodman Diagram limit, so that the allowable amplitude, Y_o, is the limit stress divided by the modal stress,

$$Y_a = \sigma_L / \sigma_m = 10\, Y_o \tag{27}$$

Thus, we may solve for the forcing function scale factor as:

$$F_m = (\lambda^T F_{unit})^{-1} (GS) Y_a / 10. \quad (28)$$

Also contained in the forcing function within STAEBL is a correction factor for the RPM effect on airfoil frequency and a correction factor for the aerodynamic excitation due to RPM change (assumed to be linearly increasing with RPM).

(Pertinent subroutine: FRCFNC)

2.4 Root Foreign Object Damage

The root foreign object damage analysis uses the same theory as derived in the initial STAEBL contract (NASA Report No. CR-167949, section 3.4.2.1-"Spanwise Bending Damage"), with the exception that the analysis uses mode shapes from the finite element analysis.

In review, the spanwise bending response was derived by considering the response to be a superposition of n natural modes of the blade, where the equilibrium equation has been decoupled into n modal equations of the form:

$$\ddot{\zeta}_k + \omega_k^2 \zeta_k = \frac{1}{m_k} P_k(t) \quad (29)$$

where $\zeta_k(t)$ is the modal amplification factor of the k'th mode,

ω_k is the natural frequency,

m_k is the modal generalized mass,

$P_k = \lambda_k$, and

[F(t)] is the modal forcing function.

Assuming that the time of load application is short relative to the time when the root stress is most critical, Equation (29) may be solved giving:

$$\zeta_k(t) = \frac{I_k}{m_k \omega_k} \sin(\omega_k t) \quad (30)$$

where I_k is the modal impulse.

Equation (30) provides the means for evaluating the blade root stresses as a function of time. Experience has shown that the highest root stresses occur at the quarter cycle of the first bending time point.

2.5 Supersonic Flutter Analysis

The capability to perform a supersonic flutter analysis for fan blades is included in the STAEBL program. The flutter analysis uses unsteady supersonic aerodynamic coefficients generated by Kaza and Kielb (Reference 7). The beam-equivalent mode shapes are used to generate the unsteady aerodynamic coefficients at a user prescribed spanwise location for the fan blade.

Once the unsteady aerodynamic coefficients have been determined, the aerodynamic work may be determined (Reference 8) as:

$$W_{TOT} = \ell\pi^2 \rho b^4 w^2 \left\{CLQ_I \bar{h}^2 + (CLA_I + CMQ_I)\, \bar{\alpha}\, \bar{h} + CMA_I \bar{\alpha}^2\right\}$$

where: ℓ is the blade span
ρ is the air density
b is the blade semichord
w is the natural frequency

CLQ, CLA, CMQ, CMA are the unsteady aerodynamic coefficients, $\bar{h}$, $\bar{\alpha}$ are the modal displacements at the pertinent span point.

Once the aerodynamic work has been determined, the logarithmic decrement may be determined as:

$$\delta = \frac{W_{TOT}}{4\, K_E}$$

where: δ is the aerodynamic logarithmic decrement
K_E is the blade average kinetic energy

(Pertinent subroutine: NASFLT)

SECTION 3.0

VALIDATION TEST CASES

As in the initial STAEBL contract, the Energy Efficient Engine shroudless fan blade design provided a design start point for the tailoring demonstrations. Dynamic resonance and flutter constraints observed in designing that blade were directly applicable to the tailored demonstration blades with the exception of the selected blade of the Energy Efficient Engine high-pressure compressor. In contrast to the optimization procedure in the initial STAEBL effort, resonance constraints were included in the first optimization attempt with each of the validation test cases (refer to NASA Report No. CR-167949, section 4.3.1). Resonance characteristics were reasonably similar; therefore, it was concluded that in each of the four test cases global optimums had been achieved.

3.1 Tailored Blades

Four validation test cases were optimized using the finite element version of STAEBL:

(1) a shroudless, superhybrid composite blade using layers of titanium, graphite epoxy and boron aluminum;

(2) a shroudless, hollow titanium blade using a composite inlay of boron titanium;

(3) a solid blade from the sixth stage of the Energy Efficient Engine high-pressure compressor; and

(4) the shroudless, superhybrid blade of (1) above, but with a variable material density and patch size at the foreign object damage impact region.

For each case, the first refined analysis generated correction factors which were applied to the approximate analysis for reoptimization. The second refined analysis confirmed that design constraints were in fact satisfied.

Two additional superhybrid blade optimizations were made to demonstrate the NASA flutter and forced response options in STAEBL.

Details of each of the demonstration test cases are provided in the following sections.

3.1.1 Superhybrid Composite Blade

Table II presents data describing the tailoring of a solid blade made of superhybrid composite material. Eleven geometric quantities were varied in this demonstration. Chord at every station was changed in proportion with root chord. The blade was sheathed with a uniform thickness titanium skin. The internal construction consisted of a uniform thickness central titanium ply with the balance being composite material, boron aluminum external to graphite epoxy. The titanium thickness and the constant fraction of boron aluminum composite were the material design variables. A minimum limit was imposed on the titanium skin thickness to avoid a maintenance penalty in excess of that recognized by the objective function. Boron and graphite fiber angles were also varied. The properties which were assumed for the composite materials are compared to Borsic (registered trademark of Avco Corporation) titanium in Table III.

The superhybrid blade root was modeled as an inward extension of the first airfoil station. This simulated the transition to a curved attachment used in hybrid construction to avoid composite plys from ending in highly stressed regions.

The TSAI-WU stress calculation has been changed to account for stresses in three dimensions rather than simply a radial direction (due to the incorporation of the finite element analysis). This has, in turn, changed the stress limits. In addition, the thickness to chord limits and other dimensional limits were relaxed (until STAEBL incorporates aerodynamic calculations into the approximate analysis, any limits chosen are arbitrary). When comparisons are made with the optimized blades in the initial STAEBL contract, these design limit changes should be remembered.

The first tailoring converged on an optimum design after fifteen iterations, using 54 percent boron aluminum (composite fibers near radial). The refined analysis results showed that approximate analysis error had permitted a minor violation of first mode flutter stability.

Due to significant changes in the initial frequency calibration factors, the second tailoring required nineteen design iterations before a new optimum could be achieved. Frequencies and correction factors are shown in Table IV. STAEBL was able to improve the design slightly over the previous optimum.

The optimized superhybrid composite blade weight and objective function showed significant reduction over the initial case. Root TSAI-WU stress, first mode 2ND flutter, first mode 2E resonance margin and second mode 4E resonance margin were either active or near active constraints.

The refined analysis indicated that the optimized superhybrid design was a valid design and judged to be acceptable. In addition, correlation between the approximate analysis and the refined analysis demonstrates that the dedicated finite element system is performing extremely well.

Table II

Superhybrid Composite Blade

Design Variables	Initial	Limits	First Tailoring	Second Tailoring
Root Chord - inches	9.119	$3. \leq b_r \leq 20.$	8.810	7.890
Thickness/Chord				
Root	0.096	$0.02 \leq t/B \leq 0.15$	0.126	0.150
25%	0.071	$0.02 \leq t/B \leq 0.15$	0.097	0.098
50%	0.054	$0.02 \leq t/B \leq 0.12$	0.061	0.106
75%	0.037	$0.02 \leq t/B \leq 0.12$	0.022	0.044
Tip	0.025	$0.02 \leq t/B \leq 0.09$	0.024	0.025
Titanium Thickness - inches				
Skin	0.050	$0.01 \leq TIS \leq 5.0$	0.034	0.021
Central	0.025	$0.0 \leq TIC \leq 5.0$	0.022	0.020
Boron Aluminum Composite	0.500	$0.0 \leq PCBA \leq 1.0$	0.544	0.591
Boron Fiber Angle - radians	0.0	$-90 \leq BAA \leq 90.$	-0.205	-0.002
Graphite Fiber Angle - radians	0.0	$-90. \leq GEA \leq 90.$	-0.712	-0.007
Blade Weight - pounds	12.000		10.959	9.73
Number of Blades	24.00		24.8	27.7
Stage Weight	288.0		271.8	269.9
Objective Function	1.271		1.247	1.211
Δ(%DOC+I):				
Engine Weight	---		---	-0.35
Engine Cost	---		---	-0.19
Maintenance Cost	---		---	+0.06
Total				-0.48
Constraints - $\Delta fn/fn$				
Resonance Margin				
First Mode 2E	0.195	$0.05 \leq MARGIN$	0.053	0.050
Second Mode 3E	0.101	$0.05 \leq MARGIN$	0.142	0.406
Second Mode 4E	0.082	$0.05 \leq MARGIN$	0.051	0.055
Third Mode 4E	0.208	$0.05 \leq MARGIN$	0.216	0.499
Flutter - Log Decrement				
First Mode	-0.030	$-0.007 \leq \delta_1$	-0.008	-0.007
Second Mode	0.013	$0.0 \leq \delta_2$	0.018	0.015
Third Mode	0.051	$0.0 \leq \delta_3$	0.064	0.056
Bird Ingestion				
Local Stress Parameter	0.160	$AVE.\epsilon \leq 0.165$	0.152	0.103
Root TSAI-WU	5.18	$RFOD \leq 28.9$	5.313	4.936
Steady Stress - psi	45,730	$\sigma \leq 47,340$	29,780	31,430
Maximum TSAI-WU Stress - psi	2.175	$\sigma \leq 1.0$	0.926 (B/A)	0.996 (B/A)

Table III

Materials Properties
(Divided By Titanium Value)

	Borsic Titanium	Adhesively Laminated Boron Aluminum	Graphite Epoxy
Elastic Modulus			
Fiber Direction	2.06	1.73	1.15
Normal Direction	1.80	1.11	0.10
Shear	3.70	1.41	0.14
Density	0.81	0.55	0.35
Strength			
Fiber Tension Direction	1.54	1.14	1.45
Fiber Compression Direction	1.54	1.64	1.45
Normal Tension Direction	0.45	0.12	0.07
Normal Compression Direction	0.45	0.26	0.23
Shear	0.47	0.20	0.16

Table IV

Superhybrid Blade Frequency Recalibration

Mode	Refined Analysis	STAEBL	Correction Factor
1	122.6	123.1	0.996
2	259.2	262.8	0.986
3	330.0	319.5	1.033

3.1.2 Hollow Blade With Composite Inlay

In Table V, data describing the tailoring of a hollow titanium blade with Borsic titanium inlay in the area of the cavity are compared with the reference blade. Thirteen geometric quantities were varied in this demonstration. Chord and thickness were defined as they were in the superhybrid blade optimization. The properties which were assumed for Borsic titanium are compared with titanium in Table III. The cavity quadrilateral /lanform boundaries are parallel to adjacent airfoil planform extremities. The cavity walls were laminates of titanium and Borsic titanium, where the titanium was of uniform thickness and was on the outer airfoil surface. The Borsic titanium was also of uniform thickness. Design variables were the distances from the cavity boundaries to the airfoil extremities and the thickness of the individual materials which comprise the cavity wall. Limits were imposed based on anticipated maintenance penalties in excess of those recognized by the objective function (the root limit ensured that the supporting attachment would be solid titanium). The Borsic fiber angle was the final variable.

The initial pass at the hollow blade optimization provided interesting results. After three design iterations, STAEBL was unable to improve on the blade design, and optimization was terminated. To determine if this design was a local minimum, another optimization pass was made, but starting with the final hollow blade of the original STAEBL effort. After ten iterations, an optimum design was found, which had a lower objective function than the previous optimum. Thus, the previous optimum may have been a local optimum. However, it is more likely that because the baseline blade was so tightly constrained, COPES/CONMIN may have had difficulty in determining a feasible direction for the optimization process to begin.

In addition, during the initial stages of STAEBL's checkout, it was found that frequency and mode shape correlations were far more accurate when the platform angle was included and the neck was properly modeled using thickened plate elements. Airfoil and neck mesh enhancements were then built into the blade preprocessor. It was also found that the use of rigid elements connecting the neck and the airfoil root substantially increased the approximate analysis accuracy and will therefore be included in the next STAEBL contract.

A refined analysis was made for the initial optimization pass and scale factors for first and second mode were relatively unchanged. Third mode was quite different, but fortunately third mode resonance was not a problem. As with the superhybrid blade, flutter calibration revealed that approximate to refined analysis correlation was very good and only minor adjustments were required for the second optimization pass to satisfy first mode 2E flutter stability. Frequencies and correction factors are shown in Table VI.

Table V

Hollow Blade With Composite Inlay

Design Variables	Initial	Limits	First Tailoring	Second Tailoring
Root Chord - inches	7.463	$3.0 \leq b_r \leq 20.0$	8.161	7.810
Thickness/Chord				
Root	0.084	$0.02 \leq t/B \leq 0.15$	0.095	0.098
25%	0.090	$0.02 \leq t/B \leq 0.15$	0.127	0.150
50%	0.056	$0.02 \leq t/B \leq 0.12$	0.058	0.067
75%	0.029	$0.02 \leq t/B \leq 0.12$	0.023	0.024
Tip	0.028	$0.02 \leq t/B \leq 0.09$	0.022	0.022
Cavity Boundaries - inches				
From Leading Edge	0.540	$0.05 \leq DLE \leq 4.5$	0.747	0.901
From Trailing Edge	1.366	$0.05 \leq DTE \leq 4.5$	1.191	1.048
From Root	2.958	$2.42 \leq DROOT \leq 16.4$	2.42	2.42
From Tip	0.250	$0.05 \leq DTIP \leq 13.0$	0.249	0.249
Cavity Wall - inches				
Titanium Skin	0.030	$0.002 \leq TTI \leq 1.0$	0.018	0.015
Composite	0.063	$0.0 \leq TLT \leq 0.30$	0.060	0.047
Borsic Fiber Angle - radians	-0.013	$-90. \leq BTA \leq 90.$	-0.013	-0.013
Blade Weight - pounds	9.698	---	9.775	8.861
Number of Blades	29.3	---	26.8	28.02
Stage Weight	284.2	---	262.0	248.3
Objective Function	1.250	---	1.173	1.079
Δ(%DOC+I):				
Engine Weight	--		--	-0.38
Engine Cost	--		--	-0.16
Maintenance Cost	--		--	-0.07
Total				-0.61
Constraints				
Resonance Margin - $\Delta fn/fn$				
First Mode 2E	0.221	$0.05 \leq MARGIN$	0.105	0.149
Second Mode 3E	0.038	$0.05 \leq MARGIN$	0.146	0.144
Second Mode 4E	0.152	$0.05 \leq MARGIN$	0.050	0.051
Third Mode 4E	0.122	$0.05 \leq MARGIN$	0.227	0.051
Flutter - Log Decrement				
First Mode	-0.071	$-0.008 \leq \delta$	-0.007	-0.008
Second Mode	0.023	$0.0 \leq \delta$	0.023	0.027
Third Mode	0.011	$0.0 \leq \delta$	0.060	0.052
Bird Ingestion				
Local Strain Parameter	0.159	AVE. $\epsilon \leq 0.165$	0.136	0.131
Root TSAI-WU	--	---	6.227	6.035
Steady Stress - psi	31,140	$\leq 47,340$	21,800	20,652
Maximum TSAI-WU Stress - psi	0.836	≤ 1.0	0.643	0.676 (Hole Borsic Titanium)

Table VI

Hollow Blade Frequency Recalibration

Mode	Refined Analysis	STAEBL	Correction Factor
1	109.9	117.3	0.937
2	242.4	263.6	0.920
3	300.1	322.3	0.931

A second optimization of the hollow blade was made and a new optimum was achieved in seven iterations. As shown in Table IV, the new design is also an improvement over the previous optimum. A refined analysis of this design showed that several elements near the base of the hollow exhibited effective stresses above the allowable. These values are caused primarily by the presence of relatively high in-plane shear stresses. In a blade, these shear stresses would result in slight local yielding, resulting in load redistribution, without structural damage to the blade. Thus, the second pass optimized hollow blade is judged to be an acceptable design.

3.1.3 Solid Compressor Blade

The high-pressure compressor inlet stage (sixth compressor stage) of the Energy Efficient Engine was selected for optimization. Design of this blade required that resonance limits be placed on the tip mode frequency for tenth harmonic excitations. A tip mode detection scheme was developed to identify the characteristic mode shape (if existent) and use its frequency in the optimization process.

The tip mode detection algorithm examines the vibratory mode shape at the blade tip. Deflection of the central nodes relative to the leading and trailing edge nodes provides the information required to determine if the mode in question is a tip vibration mode.

Table VII presents data describing the tailoring of the Energy Efficient Engine sixth stage compressor blade. Six geometric quantities were varied in this demonstration case. Chord at every station, as in the previous test cases, was changed in proportion with the root chord. Blade thicknesses were varied at five locations. A minimum tip mode margin of ± 10 percent was imposed on 10E; and for 2, 3 and 4E, a minimum resonance margin of ± 5 percent was required for modes one through four.

Table VII

Optimization of Energy Efficient Engine
Sixth Stage Compressor Blade

	Initial	Second Tailoring
Root Chord - inches	2.807	1.710
Thickness/Chord		
Root	0.102	0.135
25%	0.008	0.119
50%	0.007	0.008
75%	0.004	0.004
Tip	0.004	0.005
Foil Weight - pounds	0.431	0.191
Number of Blades	26.0	42.7
Stage Weight (Objective Function) - pounds	11.2	8.141
First Mode 2E	0.207	0.051
Second Mode 4E	0.524	0.140
Tip Mode 10E	0.127	0.138
Flutter (First Mode Bending)	0.528	0.994 (must be $\leqslant$1.0)
Active Constraints	None	2E First Mode

The first optimization pass of the solid blade required five iterations but did not use a flutter constraint. Later, when first pass calibration calculations were made, flutter stability was found to be violated, and chord length reduction was shown to be excessive. To avoid the flutter instability problem with the next optimization pass, a reduced velocity parameter previously established for the inlet stage of the Energy Efficient Engine was used as a flutter constraint.

Table VIII shows frequency comparisons between STAEBL's approximate analysis and the NASTRAN refined analysis for the first three modes and the tip mode of the sixth stage blade. The 11 percent discrepancy for the second mode frequency was demonstrated to be the manner in which the airfoil root is presently attached to the extended neck, i.e., without offsets. As with the hollow blade design, when the neck to airfoil junction was properly modeled in NASTRAN with rigid elements, correlations between coarse and fine meshes were excellent. For the sixth stage blade, correlation was within 3 percent for the first three modes of vibration.

When the sixth stage blade was optimized using the STAEBL system, the blade chord was reduced by nearly 40 percent as shown in Table VII. The objective function, being stage weight, was reduced by nearly 30 percent.

Table VIII

Frequency Comparison, Energy Efficient Engine
Sixth Stage Compressor

Mode	STAEBL Approximate Analysis	NASTRAN Refined Analysis
1	587.3	576.5
2	1489.1	1341.2
3	1682.7	1660.4
Tip	2351.4	2674.1

3.1.4 Superhybrid Blade With Local Increased Density

The last validation test case was the superhybrid blade with an increased local density patch. The local density of the patch was treated as a no-stiffness add-on to the original element densities. The patch location is defined using five design variables: a density, patch distances from root and tip, and distance from leading and trailing edges.

The optimization, shown in Table IX, commenced with an intermediate superhybrid design to which a 1.5 pound patch mass was added.

STAEBL optimization proceeded for 21 design iterations, until it halted due to optimum design convergence. The final design is very similar to the final superhybrid configuration, although 1.1 pounds of patch material remains in the blade. However, the objective function with the patch, 1.27, is higher than that of the optimum superhybrid blade, 1.21. Therefore, a superior local density configuration would be to completely eliminate the added mass. The iteration scheme of STAEBL, COPES/CONMIN, apparently finds it difficult to completely eliminate a design variable, although, as in this instance, noticable improvement may develop through the elimination.

Table IX

Optimization of Superhybrid Blade
With Increased Local Density

	Initial	Final
Root Chord - inches	11.115	7.843
Thickness/Chord		
Root	0.097	0.150
25%	0.072	0.124
50%	0.078	0.142
75%	0.040	0.065
Tip	0.034	0.031
Titanium Thickness - inches		
Skin	0.043	0.015
Center	0.023	0.019
$\%_{B/A}$	72.33	64.65
$\theta_{B/A}$ - degrees	-0.002	-0.002
$\theta_{G/E}$ - degrees	-0.007	-0.007
Local Mass/Area - lb sec^2/in^3	0.000020	0.000015
AD_{LE} - inches	0.94	0.976
AD_{TE} - inches	0.94	0.973
AD_{ROOT} - inches	10.0	11.637
AD_{TIP} - inches	0.2	0.201
Foil Weight - pounds	20.81	10.54
Number of Blades	19.7	27.9
Stage Weight - pounds	409.8	294.2
Object Function	1.797	1.275
Active Constraints	2nd Mode 4E Root Stress	2nd Mode 3E Resonance, Root t/b

3.2 Additional Optimization Test Cases

3.2.1 Superhybrid Blade With NASA Flutter Code

To verify the successful installation of the NASA flutter code and the forced response analysis, a superhybrid blade was optimized using each of these STAEBL options. The optimum blade using the NASA flutter code is similar to that derived using the Pratt & Whitney flutter code, but somewhat lighter, with a stage weight of 239 pounds compared with the original at 270 pounds.

3.2.2 Superhybrid Blade With Forced Response

The forced response analysis proved to be a more restrictive design procedure (see Table X). This is due to the coupling of steady and vibratory stresses. Using the forced response option, the optimum stage weight was determined to be 326 pounds.

Table X

Superhybrid Blade Using Forced Response Option

	Initial	Final
Root Chord - inches	11.115	9.153
Thickness/Chord - inches		
Root	0.097	0.131
25%	0.062	0.077
50%	0.062	0.080
75%	0.029	0.037
Tip	0.023	0.026
Titanium Thickness - inches		
Skin	0.043	0.038
Center	0.023	0.022
$\%_{B/A}$	72.33	67.5
$\theta_{B/A}$ - degrees	-0.002	-0.002
$\theta_{G/E}$ - degrees	-0.007	-0.007
Foil Weight - pounds	19.27	13.63
Number of Blades	19.7	23.9
Stage Weight - pounds	379.4	325.9
Object Function	1.728	1.434
Resonance Margin - $\Delta fn/fn$		
First Mode 2E		0.080
Second Mode 3E		0.366
Second Mode 4E		0.024
Third Mode 4E		0.386

SECTION 4.0

COMPUTATIONAL EFFICIENCY

Both analytical accuracy and computational efficiency have been important factors in the design of STAEBL. Accuracy of the approximate analytical models has been demonstrated with refined models of the validation test cases. In addition, the test cases have shown that STAEBL can arrive at optimum blade designs with minimal user effort and at relatively low CPU (central processing unit) times.

In this section the computational efficiency of STAEBL is discussed with regard to:

1. the finite element analysis,

2. enhancements made to the main subroutine to decrease design iteration time, and

3. a method of determining the approximate CPU time requirement for typical optimization cases.

4.1 Approximate Finite Element Analysis

The approximate finite element stress and vibration analysis is the cornerstone of STAEBL's approximate optimization procedure, providing evaluations of the blade weight, stresses, frequencies, and mode shapes for objective and constraint evaluations, as well as for later flutter and impact analyses. Due to the importance of this analysis, it is essential that accuracy be attained in as efficient a manner as possible.

To maximize the efficiency of accurate approximate finite element analysis, a specialized code was constructed. This code is geared directly toward efficient extraction of prestressed blade frequencies. Reduced integration element technology provides computationally efficient plate finite elements. In-core matrix storage and execution, appropriate for a small capacity analysis, provide efficient finite element analysis by minimizing disk input/output requirements. Application of the Guyan Reduction has proven to significantly speed eigenvalue extraction with negligible loss of accuracy. Finally, the IMSL (International Mathematical and Statistical Library) subroutine employed in STAEBL provided for efficient matrix decomposition, forward and backward substitution, and eigenvalue extraction.

4.2 Optimization Control System Enhancement

Based on discussions with G. N. Vanderplaats, alterations were made to the STAEBL optimization control system to improve analysis efficiency. Initially, values for the objective function and all violated, active and inactive constraints were evaluated. By removing inactive constraint gradient calculations, significant time savings in the optimization process were realized (in some cases, execution time was reduced as much as 50 percent). All analyses are, however, referenced during a design move.

4.3 Approximate CPU Time Requirements

Central processing unit (CPU) requirements are dependent on both the computer and the data input/output disk setup. The following CPU estimates were made based on an IBM 3081 computer with an efficient input/output system. Execution times summarized below were calculated using developmental and validation test cases. In general:

1. Typical optimizations for fans require approximately twelve seconds per iteration per design variable. For example, a hollow blade with the Pratt & Whitney flutter code requires an estimated 10 iterations with 13 design variables. The execution time is determined in the following manner:

   12 x 10 x 13 = 1560 seconds, or 26.0 minutes
   actual execution time was 26.6 minutes.

2. A solid blade with no foreign object damage and time consuming flutter calculation (low- or high-pressure compressor blades) requires six seconds per iteration per design variable.

Several trial runs will be required to determine adjustment factors to adequately predict execution times on different systems.

SECTION 5.0

REFERENCES

1. MacNeal, R. H., "A Simple Quadrilateral Shell Element," Computers & Structures, Vol. 8, Pergamon Press, Great Britain, 1978, pp. 175-183.

2. Guyan, R. J., "Reduction of Stiffness and Mass Matrices," AIAA Journal, Vol. 3,2, February 1965.

3. MacNeal, R. H., The NASTRAN Theoretical Manual, NASA Sp-221 (01), April 1972.

4. Jones, R. M., Mechanics of Composite Materials, Scripta Book Co, Washington, D.C., 1975.

5. Tsai, S. W. and Wu, E. M., "A General Theory of Strength for Anisotropic Materials," J. Composite Materials, Vol. 5 (Jan., 1971), pp 58-80.

6. Thompson, William T., Theory of Vibration with Applications, Prentice-Hall, Inc., Englewood Cliffs, New Jersey, 1972.

7. Kaza, K. R. and R. E. Kielb, "Flutter and Response of a Mistuned Cascade in Incompressible Flow," AIAA Journal, Vol. 20, No. 8, August 1982, pp. 1120-1127.

8. Carta, F. O., "Coupled Blade-Disk-Shroud Flutter Instabilities in Turbojet Engine Rotors," J. Eng Power, Vol. 89, July 1967, pp. 419-426.

APPENDIX

PRATT & WHITNEY PROPRIETARY SUPERSONIC FLUTTER ANALYSIS

- For NASA Use Only -

As an option of STAEBL, a Pratt & Whitney proprietary supersonic flutter analysis is available for NASA use only. The optional flutter analysis is referenced when more than one spanwise strip is requested for flutter analysis (NAC on card C3). With the optional flutter analysis, multiple strips may be evaluated to determine the overall blade stability. In all other respects, the analysis is similar to the analysis performed by the Kaza and Kielb flutter code that is publicly available.

Use of the Pratt & Whitney flutter code increases the time per iteration by approximately three seconds.

(Pertinent subroutine: MNW751)

DISTRIBUTION LIST

NASA-Lewis Research Center
21000 Brookpark Road
Cleveland, OH 44135
Attn: Contracting Officer, MS 500-13

NASA-Lewis Research Center
21000 Brookpark Road
Cleveland, OH 44135
Attn: L. J. Kiraly, MS 23-2

NASA-Lewis Research Center
21000 Brookpark Road
Cleveland, OH 44135
Attn: Tech. Rept. Cont. Office, MS 60-1

NASA-Lewis Research Center
21000 Brookpark Road
Cleveland, OH 44135
Attn: C. C. Chamis, MS 49-6 (6 copies)

NASA-Lewis Research Center
21000 Brookpark Road
Cleveland, OH 44135
Attn: Tech. Utilization Office, MS 7-3

NASA-Lewis Research Center
21000 Brookpark Road
Cleveland, OH 44135
Attn: M. S. Hirschbein, MS 49-8

NASA-Lewis Research Center
21000 Brookpark Road
Cleveland, OH 44135
Attn: AFSC Liason Office, MS 501-3

NASA-Lewis Research Center
21000 Brookpark Road
Cleveland, OH 44135
Attn: J. A. Ziemianski, MS 86-1

NASA-Lewis Research Center
21000 Brookpark Road
Cleveland, OH 44135
Attn: Division Contract File
MS 49-6 (2 copies)

NASA-Lewis Research Center
21000 Brookpark Road
Cleveland, OH 44135
Attn: P. B. Burstadt, MS 100-5

NASA-Lewis Research Center
21000 Brookpark Road
Cleveland, OH 44135
Attn: Library, MS 60-3

NASA-Lewis Research Center
21000 Brookpark Road
Cleveland, OH 44135
Attn: D. P. Fleming, MS 6-1

NASA-Lewis Research Center
21000 Brookpark Road
Cleveland, OH 44135
Attn: L. Burke, MS 46-6

NASA-Lewis Research Center
21000 Brookpark Road
Cleveland, OH 44135
Attn: R. E. Kielb, MS 23-2

NASA-Lewis Research Center
21000 Brookpark Road
Cleveland, OH 44135
Attn: R. H. Johns, MS 49-8

NASA-Lewis Research Center
21000 Brookpark Road
Cleveland, OH 44135
Attn: J. J. Adamczyk, MS 5-9

DISTRIBUTION LIST (continued)

NASA-Lewis Research Center
21000 Brookpark Road
Cleveland, OH 44135
Attn: R. D. Hager, MS 86-7

National Aeronautics &
Space Administration
Washington, DC 20546
Attn: NHS-22/Library

National Aeronautics &
Space Administration
Washington, DC 20546
Attn: RTM-6/S. L. Venneri

NASA Ames Research Center
Moffett Field, CA 94035
Attn: Library, MS 202-3

NASA Goddard Space Flight Center
Greenbelt, MD 20771
Attn: 252/Library

NASA John F. Kennedy Space Center
Kennedy Space Center, FL 32931
Attn: Library, AD-CSO-1

NASA Langley Research Center
Hampton, VA 23665
Attn: Library, MS 185

NASA Langley Research Center
Hampton, VA 23665
Attn: M. F. Card, MS 244

NASA Langley Research Center
Hampton, VA 23665
Attn: W. J. Strout

NASA Lyndon B. Johnson Space Center
Houston, TX 77001
Attn: JM6/Library

NASA George C. Marshall Space
Flight Center
Marshall Space Flt. Center, AL 35812
Attn: AS61/Library

NASA George C. Marshall Space
Flight Center
Marshall Space Flt. Center, AL 35812
Attn: R. S. Ryan

Jet Propulsion Laboratory
4800 Oak Grove Drive
Pasadena, CA 91103
Attn: Library

Jet Propulsion Laboratory
4800 Oak Grove Drive
Pasadena, CA 91103
Attn: B. Wada

Jet Propulsion Laboratory
4800 Oak Grove Drive
Pasadena, CA 91103
Attn: R. Levi

NASA S&T Information Facility
P. O. Box 8757
Baltimore-Washington Int. Airport, MD 21240
Attn: Acquisition Dept. (10 copies)

Air Force Aeronautical Propulsion Laboratory
Wright-Patterson AFB, OH 45433
Attn: Z. Gershon

Air Force Aeronautical Propulsion Laboratory
Wright-Patterson AFB, OH 45433
Attn: N. Khot

DISTRIBUTION LIST (continued)

Air Force Systems Command
Aeronautical Systems Division
Wright-Patterson AFB, OH 45433
Attn: Library

Air Force Systems Command
Aeronautical Systems Division
Wright-Patterson AFB, OH 45433
Attn: C. W. Cowie

Air Force Systems Command
Aeronautical Systems Division
Wright-Patterson AFB, OH 45433
Attn: J. McBane

Aerospace Corporation
1400 E. El Segundo Blvd.
Los Angeles, CA 90045
Attn: Library-Documents

Air Force Office of Sci. Research
Washington, DC 20333
Attn: A. K. Amos

Department of the Army
U. S. Army Material Command
Washington, DC 20315
Attn: AMCRD-RC

U. S. Army Ballistics Research Lab.
Aberdeen Proving Ground, MD 21005
Attn: Dr. Donald F. Haskell
MS DRXBR-BM

Mechanics Research Laboratory
Army Materials & Mech. Research Ctr.
Watertown, MA 02172
Attn: Dr. Donald W. Oplinger

U. S. Army Missile Command
Redstone Scientific Info. Center
Redstone Arsenal, AL 35808
Attn: Document Section

AFFDL/FBE
Wright-Patterson AFB, OH 45433
Attn: D. W. Smith

Commanding Officer
U. S. Army Research Office (Durham)
Box CM, Duke Station
Durham, NC 27706
Attn: Library

Bureau of Naval Weapons
Department of the Navy
Washington, DC 20360
Attn: RRRE-6

Commander, U. S. Naval Ord. Lab.
White Oak
Silver Springs, MD 20910
Attn: Library

Director, Code 6180
U. S. Naval Research Laboratory
Washington, DC 20390
Attn: Library

Denver Federal Center
U. S. Bureau of Reclamation
P. O. Box 25007
Denver, CO 80225
Attn: P. M. Lorenz

Naval Air Propulsion Test Center
Aeronautical Engine Department
Trenton, NJ 08628
Attn: Mr. James Salvino

DISTRIBUTION LIST (continued)

Naval Air Propulsion Test Center
Aeronautical Engine Department
Trenton, NJ 08628
Attn: Mr. Robert DeLucia

Federal Aviation Administration
Code ANE-214, Propulsion Section
12 New England Executive Park
Burlington, MA 01803
Attn: Mr. Robert Berman

Federal Aviation Administration DOT
Office of Aviation Safety, FOB 10A
800 Independence Ave., SW
Washington, DC 20591
Attn: Mr. John H. Enders

FAA, ARD-520
2100 Second Street, SW
Washington, DC 20591
Attn: Commander John J. Shea

National Transportation Safety Board
800 Independence Avenue, SW
Washington, DC 20594
Attn: Mr. Edward P. Wizniak, MS TE-20

Arizona State University
Dept. of Aerospace Engrg. & Engrg. Sci.
Tempe, AZ 85281
Attn: H. D. Nelson

Rockwell International Corporation
Los Angeles International Airport
Los Angeles, CA 90009
Attn: Mr. Joseph Gausselin
D422/402 AB71

Rensselaer Polytechnic Institute
Troy, NY 12181
Attn: R. Loewy

Cleveland State University
Dept. of Civil Engineering
Cleveland, OH 44115
Attn: P. Bellini

Massachusetts Institute
of Technology
Cambridge, MA 02139
Attn: K. Bathe

Massachusetts Institute
of Technology
Cambridge, MA 02139
Attn: T. H. Pian

Massachusetts Institute
of Technology
Cambridge, MA 02139
Attn: J. Mar

Massachusetts Institute
of Technology
Cambridge, MA 02139
Attn: E. A. Witme

Massachusetts Institute
of Technology
Cambridge, MA 02139
Attn: J. Dugundji

Univ. of Illinois at Chicago Center
Department of Materials Engineering
Box 4348
Chicago, IL 60680
Attn: Dr. Robert L. Spilker

Detroit Diesel Allison
General Motors Corporation
Speed Code T3, Box 894
Indianapolis, IN 46206
Attn: Mr. William Springer

DISTRIBUTION LIST (continued)

General Motors Corporation
Warren, MI 48090
Attn: R. J. Trippet

AVCO Lycoming Division
550 South Main Street
Stratford, CT 06497
Attn: Mr. Herbert Kaehler

Beech Aircraft Corp., Plant 1
Wichita, KA 67201
Attn: Mr. M. K. O'Connor

Bell Aerospace
P. O. Box 1
Buffalo, NY 14240
Attn: R. A. Gellatly

Boeing Aerospace Company
Impact Mechanics Lab
P. O. Box 3999
Seattle, WA 98124
Attn: Dr. R. J. Bristow

Boeing Commercial Airplane Company
P. O. Box 3707
Seattle, WA 98124
Attn: Dr. Ralph B. McCormick

Boeing Commercial Airplane Company
P. O. Box 3707
Seattle, WA 98124
Attn: Mr. David T. Powell, MS 73-01

Boeing Commercial Airplane Company
P. O. Box 3707
Seattle, WA 98124
Attn: Dr. John H. Gerstle

Boeing Company
Wichita, KA 67201
Attn: Library

McDonnell Douglas Aircraft Corporation
P. O. Box 516
Lambert Field, MO 63166
Attn: Library

Douglas Aircraft Company
3855 Lakewood Blvd.
Long Beach, CA 90846
Attn: Mr. M. A. O'Connor, Jr.
MS 36-41

Garrett AiResearch Manufacturing Co.
111 S. 34th Street, P. O. Box 5217
Phoenix, AZ 85010
Attn: L. A. Matsch

Mr. R. Stockton
Garrett Turbine Engine Company
Rotor Integrity, 503-42
Mechanical Component Design
111 S. 34th Street, P. O. Box 5217
Phoenix, AZ 85010

General Dynamics
P. O. Box 748
Fort Worth, TX 76101
Attn: Library

General Dynamics/Convair Aerospace
P. O. Box 1128
San Diego, CA 92112
Attn: Library

General Electric Company
Interstate 75, Bldg. 500
Cincinnati, OH 45215
Attn: Dr. L. Beitch, MS K221

General Electric Company
Interstate 75, Bldg. 500
Cincinnati, OH 45215
Attn: Dr. M. Roberts, MS K221

General Electric Company
Interstate 75, Bldg. 500
Cincinnati, OH 45215
Attn: Dr. V. Gallardo, MS K221

DISTRIBUTION LIST (continued)

General Electric Company
Aircraft Engine Group
Lynn, MA 01902
Attn: Mr. Herbert Garten

Grumman Aircraft Engrg. Corp.
Bethpage, Long Island, NY 11714
Attn: Library

Grumman Aircraft Engrg. Corp.
Bethpage, Long Island, NY 11714
Attn: H. A. Armen

IIT Research Institute
Technology Center
Chicago, IL 60616
Attn: Library

Lockheed California Company
P. O. Box 551
Dept. 73-31, Bldg. 90, PL. A-1
Burbank, CA 91520
Attn: Mr. D. T. Pland

Lockheed California Company
P. O. Box 551
Dept. 73-71, Bldg. 63, PL. A-1
Burbank, CA 91520
Attn: Mr. Jack E. Wignot

Northern Space Laboratories
3401 West Broadway
Hawthorne, CA 90250
Attn: Library

North American Rockwell, Inc.
Rocketdyne Division
6633 Canoga Avenue
Canoga Park, CA 91304
Attn: Library, Dept. 596-306

North American Rockwell, Inc.
Rocketdyne Division
6633 Canoga Avenue
Canoga Park, CA 91304
Attn: J. F. Newell

North American Rockwell, Inc.
Space & Information Systems Div.
12214 Lakewood Blvd.
Downey, CA 90241
Attn: Library

Norton Company
Industrial Ceramics Div.
Armore & Spectramic Products
Worcester, MA 01606
Attn: Mr. George E. Buron

Norton Company
1 New Bond Street
Industrial Ceramics Division
Worcester, MA 01606
Attn: Mr. Paul B. Gardner

Aeronautical Research Association of
Princeton, Inc.
P. O. Box 2229
Princeton, NJ 08540
Attn: Dr. Thomas McDonough

Republic Aviation
Fairchild Hiller Corporation
Farmington, Long Island, NY
Attn: Library

Rohr Industries
Foot of H Street
Chula Vista, CA 92010
Attn: Mr. John Meaney

TWA, Inc.
Kansas City International Airport
P. O. Box 20126
Kansas City, MO 64195
Attn: Mr. John J. Morelli

DISTRIBUTION LIST (continued)

Stevens Institute of Technology
Castle Point Station
Hoboken, NJ 07030
Attn: F. Sisto

Stevens Institute of Technology
Castle Point Station
Hoboken, NJ 07030
Attn: A. T. Chang

Mechanical Technologies Inc.
Latham, NY
Attn: M. S. Darlow

Shaker Research Corporation
Northway 10, Executive Park
Ballston Lake, NY 12019
Attn: L. Lagace

Lockheed Palo Alto Research Labs
Palo Alto, CA 94304
Attn: B. O. Almroth

Lockheed Missiles and Space Company
Huntsville Research & Engrg. Center
P. O. Box 1103
Huntsville, AL 18908
Attn: H. B. Shirley

MacNeal-Schwendler Corporation
7442 North Figueroa Street
Los Angeles, CA 90041
Attn: R. H. MacNeal

MARC Analysis Research Corporation
260 Sheridan Avenue, Suite 314
Palo Alto, CA 94306
Attn: J. Nagtegaal

Ohio State University
Columbus, OH 43210
Attn: A. W. Leissa

University of California
Mechanics & Structures Department
School of Engrg. & Applied Sciences
Los Angeles, CA 90024
Attn: L. A. Schmit, Jr.

Columbia University
New York, NY 10027
Attn: R. Vaicaitis

Georgia Institute of Technology
School of Civil Engineering
Atlanta, GA 30332
Attn: S. N. Atluri

Georgia Institute of Technology
225 North Avenue
Atlanta, GA 30332
Attn: G. J. Simitsis

Lawrence Livermore Laboratory
P. O. Box 808, L-421
Livermore, CA 94550
Attn: Library

Lehigh University Institute of
Fracture and Solid Mechanics
Bethlehem, PA 18015
Attn: G. T. McAllister

Materials Science Corporation
1777 Walton Road
Blue Bell, PA 19422
Attn: W. B. Rosen

DISTRIBUTION LIST (continued)

National Bureau of Standards
Engineering Mechanics Section
Washington, DC 20234
Attn: R. Mitchell

Purdue University
School of Aeronautics & Astronautics
West Lafayette, IN 47907
Attn: C. T. Sun

University of Dayton
Research Institute
Dayton, OH 45409
Attn: F. K. Bogner

Texas A&M University
Aerospace Engineering Department
College Station, TX 77843
Attn: W. E. Haisler

Texas A&M University
Aerospace Engineering Department
College Station, TX 77843
Attn: J. M. Vance

V. P. I. and State University
Department of Engineering Mechanics
Blacksburg, VA 24061
Attn: R. H. Heller

United Technologies Corporation
Government Products Division
P. O. Box B2691
West Palm Beach, FL 33402
Attn: Library, 706-50

United Technologies Corporation
Pratt & Whitney
Engineering Division-North
400 Main Street
East Hartford, CT 06108
Attn: K. W. Brown, 163-10

University of Arizona
College of Engineering
Tucson, AZ 87521
Attn: H. Kamel

University of Arizona
College of Engineering
Tucson, AZ 87521
Attn: J. C. Heinrich

University of California
Department of Civil Engineering
Berkeley, CA 94720
Attn: E. Wilson

University of Kansas
School of Engineering
Lawrence, KS 66045
Attn: R. H. Dodds

University of Virginia
School of Engrg. & Applied Science
Charlottesville, VA 22901
Attn: E. J. Gunter

Northwestern University
Department of Civil Engineering
Evanston, IL
Attn: T. Belytschko

United Technologies Corporation
Government Products Division
P. O. Box B2691
West Palm Beach, FL 33402
Attn: R. A. Marmol, 713-39

United Technologies Corporation
Pratt & Whitney
Engineering Division-North
400 Main Street
East Hartford, CT 06108
Attn: Library, 169-31

DISTRIBUTION LIST (continued)

United Technologies Corporation
Pratt & Whitney
Engineering Division-North
400 Main Street
East Hartford, CT 06108
Attn: R. Liss, 163-09

United Technologies Corporation
Pratt & Whitney
Engineering Division-North
400 Main Street
East Hartford, CT 06108
Attn: D. H. Hibner, 163-09

United Technologies Corporation
Hamilton Standard Division
Windsor Locks, CT 06096
Attn: Dr. G. P. Towsend

United Technologies Corporation
Hamilton Standard Division
Windsor Locks, CT 06096
Attn: Dr. R. A. Cornell

United Technologies Corporation
United Technologies Research Center
East Hartford, CT 06108
Attn: Dr. A. Dennis